Revisiting the Strong and Weak ENSO Teleconnection Impacts using a High-Resolution Atmospheric Model

Muhammad Mubashar Ahmad Dogar[1, 2*], and Mansour Almazroui[3, 4]

ABSTRACT

To evaluate the performance of a high-resolution atmospheric model (HiRAM) and to improve our understanding of the climatic impacts of ENSO forcing and associated teleconnections, we analyzed AMIP style HiRAM simulations conducted effectively at 25 km grid spacing. To better assess HiRAM response to ENSO climate variability; we categorized it into strong and weak El Niño/La Niña episodes. The HiRAM model reproduced the impacts of strong ENSO over global scale very well, however, it underestimated ENSO teleconnection patterns and associated changes over regional scale (e.g., MENA and South Asia), especially following weak ENSO that could be attributed to model weak response to circulation changes such as Pacific North American (PNA) and North Atlantic Oscillation (NAO). Moreover, our results emphasize that ENSO impacts are relatively stronger over the Inter-Tropical Convergence Zone (ITCZ) compared to extratropics and high-latitude regions. The positive phase of ENSO causes weakening in rainfall over the African tropical rain-belt, parts of South and Southeast Asia. Both the reanalysis and HiRAM results reveal that ENSO-induced negative (positive) NAO-like response and associated changes over Southern Europe and North Africa vary significantly following the increased intensity of El Niño (La Niña). We further found that the ENSO magnitude significantly impacts Hadley and Walker circulations. The El Niño phase of ENSO overall strengthens the Hadley Cell, and the reverse is true for the La Niña phase. This ENSO-induced strengthening and weakening of Hadley Cell induce significant impact over South Asian and African convective regions through modification of the ITCZ circulation system.

Key words: ENSO, El Nino/La Nina, NAO, MENA, Hadley Circulation, ITCZ, Monsoon System.

1. Global Change Impact Studies Centre, Ministry of Climate Change, Islamabad, Pakistan
2. Graduate School of Environmental Science, Hokkaido University, Sapporo, Japan
3. Center of Excellence for Climate Change Research/Department of Meteorology, King Abdulaziz University, Jeddah, Saudi Arabia
4. Climate Research Unit, School of Environmental Sciences, University of East Anglia, Norwich, United Kingdom

*mubashardogar@yahoo.com

1. Introduction

El Niño–Southern Oscillation (ENSO) is an interannual climate variability pattern that has tremendous affects on the climate of the tropical and subtropical regions (Trenberth et al. 1998; Timmermann et al. 1999; Neelin et al. 1998; Trenberth and Caron, 2000; Lee et al. 2010, 2012; Zhang et al. 2011). The warming and cooling phases of this Pacific inter-annual variability are termed as El Niño and La Niña respectively. Both these phases have worldwide climatic interactions with important ecological and socioeconomic implications (Timmermann et al., 1999).

The physical link between ENSO variability and associated temperature, precipitation and wind changes at the global and regional scale has been assessed in many studies (Timmermann et al., 1999; Trenberth et al., 1998; Diaz et al., 2001; Ashok et al. 2001, 2004; Molteni et al., 2003; Bracco et al., 2007, Kucharski et al., 2013; Kripalani et al., 2007; Dogar et al., 2019; Dogar and Shahid, 2019). Several past studies have shown a strong correlation between Eastern and Central Equatorial Pacific sea surface temperature variability and rainfall pattern over the Pacific, Atlantic, Indian Ocean and associated continental regions with focus on South Asia, Southeast Asia and Africa (Lee et al., 2010; Kucharski et al. 2013; Zhang et al., 2011, 2012, 2013; Afzaal et al., 2013; Wang et al. 2012; Rasmusson and Carpenter, 1983]. ENSO is known to be the largest climatic forcing which deals with variability of interannual monsoon system through the large-scale east-west displacement of heat transfer in the tropics (Kumar et al. 1999a]).

Many recent studies have shown that the American, Asian, Indian, and Australian rainfall systems are greatly influenced by the ENSO teleconnection (Lau et al., 2000; Bracco et al., 2007; Lean et al., 2008; Kripalani et al., 2007). Numerous studies have shown the simultaneous association of ENSO-indices and the rainfall over India (Pant and Parthasarathy, 1987; Ashok et al. 2001, 2004; Kripalani et al. 2007; Wu et al., 2012). Using observation and reanalysis products, Singh et al. (2013) investigated the mechanisms and teleconnections behind the long-term variability in the Indian Ocean SST, with a particular focus on SST in the southwestern Indian Ocean tropics. This study concludes that boral winter (DJF) SST is highly dependent on long-lived La Niña impacts, indicating the importance of SSTs in the Indian Ocean, in addition to SSTs in the Pacific, to better represent ENSO-induced teleconnections.

The original idea describing physical connection between ENSO forcing and South Asian monsoon system, in particular the Indian monsoon, through large-scale dynamic circulation was initially proposed by Gilbert Walker (Walker, 1925). Subsequently, several studies have shown that the warm phase (El Niño) leads to the weakening of the Indian monsoon system with an overall decrease in precipitation (Bhalme and Mooley, 1980; Rasmusson and Carpenter, 1983; Shukla and Paolino, 1983; Ju and Slingo, 1995; Ashok et al. 2001, 2004; Dogar et al., 2017a). Conversely, the cold phase (La Niña) is associated with an intensification of the Indian monsoon system and increased precipitation [Shukla and Paolino 1983; Joo and Slingo, 1995). Many other studies have also discussed the variations in the relationships between monsoonal rainfall and its predictors

(Parthasarathy et al., 1991a, 1992, 1994; Ashok et al. 2001). These variations are attributed to change in ENSO characteristics such as period and amplitude (Kumar et al. 1999b).
Previous studies have shown that the ENSO, which originates in the central Pacific and in the east Pacific, has significant variations and nonlinearities in its pattern, strength and associated climatic impacts (Frauen et al., 2014; Chung et al., 2013; Hoerling et al., 1997; Wu et al., 2020; Wu and Zhuoqi, 2019). However, it is difficult to distinguish weather these are caused by the different signs/types, strengths, or spatial patterns of such events (e.g., strong or weak El Niño events or by combinations of these).

In the past couple of decades, there has been an increase in both frequency and strength of El Niño (La Niña) events with maximum warming (cooling) occurring in the central equatorial Pacific (e.g., Latif et al., 1997; Afzaal et al., 2013; Lee et al., 2010). This is called as Central Pacific (CP) El Niño (Yu and Kim, 2010; Kao and Yu, 2009), dateline El Niño (Larkin and Harrison, 2005), El Niño Modoki (Ashok et al., 2007) or warm pool El Niño (Kug et al. 2009). While previous studies on ENSO events have discussed an increasing frequency of El Niño and La Niña events in recent decades (Yeh et al. 2009; Lee et al. 2010; Timmermann et al., 1999), studies on the magnitude and nonlinearity of El Niño and La Niña events are still evolving, and require further research. Therefore, there is a need to look at the strength of ENSO variability and associated global and regional climatic impacts. Being an important and leading mode of interannual climate variability, El Niño Southern Oscillation produces significant impacts on global and regional climate; hence there is a great interest in studying how the magnitude of the tropical Pacific sea surface temperature would affect tropical global climate patterns (including large scale circulations) and related changes in temperature and precipitation distribution.

Although the existence of the Hadley cell and its sensitivity to ENSO episodes has been extensively investigated (Held and Hou 1980; Seager et al. 2003; Feng and Li, 2013; Nguyen et al., 2013), questions remain, as to how this thermally driven large-scale tropical Hadley circulation will respond to ENSO strength (i.e., strong and weak ENSO). For this purpose, we will make use of a high-resolution atmospheric model, HiRAM with a resolution that generally is used by regional climate models in climate downscaling studies for better representation of regional climate processes influenced by global scale patterns. The HiRAM has effectively been used to study global and regional climatic changes (Bangalath et al., 2015; Dogar et al., 2017b; Dogar, 2018; Dogar and Shahid, 2018; Dogar, 2020). In this study, we will see how well it can reproduce the impact of strong and weak ENSO events at the global and regional scale. The use of high-resolution modeling technique provides us a unique opportunity to examine how the ENSO-induced circulation anomalies at various scales influence regional climate. To the best of our knowledge, there is rarely any study pertaining to regional ENSO impacts using a Global Climate Model (GCM) at a spatial resolution of about 25 km or better; hence, in this sense this study is very useful for its successors. Besides, this version of HIRAM is effective in overcoming many of the limitations encountered by coarse-resolution GCMs and RCMs. Due to their fine grid spacing, important processes such as large-scale condensation, land-sea interaction, and topographical forcing are better resolved in high-resolution GCMs (Boyle & Klein, 2010; Lau & Ploshay, 2009; Harris et al., 2016). Recent studies further emphasized that the regional convective structure and precipitation change are very sensitive to the model horizontal resolution (Bui et al., 2019; Liu, Yu, & Chen, 2018). The idea of conducting HIRAM AMIP simulations is to see if there could be any improvement in the simulations of ENSO response especially at regional scale with improved resolution.

As Hadley circulation transport energy from equator to poleward and drives the climate of tropics and extratropics. Hence, the main purpose of studying the magnitude of ENSO events is to investigate the impact of El Niño/La Niña strength on the Hadley circulation and subsequent temperature and precipitation distribution at the global and regional scale focusing on the tropics and extratropics. We will also revisit ENSO-induced variation in temperature and precipitation over the Middle East and North Africa (MENA) with focus on Arabian Peninsula in winter season as this region is getting attention and have been focused in many studies (Kucharski et al., 2013; Zeng and Ning 2003, Giannini et al., 2008; Dogar, 2019) because of its sensitivity and drought-like response to such events. In addition, we will focus on the model performance in replicating known facts of ENSO teleconnection pattern over Pacific and Atlantic region such as ENSO-induced PNA pattern over the Pacific as well as ENSO-induced NAO-like pattern in North Atlantic region and associated climatic effects particularly in Europe and Middle East region.

Therefore, the current paper deals with the comparative study of ENSO teleconnection over ITCZ and extratropical regions and its effect on rainfall, particularly in Africa and the Middle East extending to the East Asian region. The study also deals with the ENSO-induced modulation (i.e., strengthening or weakening) of Hedley and Walker circulations that could initiate a significant impact on Indian, Middle Eastern and African rainfall distribution. The rest of the paper is organized as follows. Section 2 discusses material and methods including the description of the model used in this study. Strong and weak ENSO episodes and their global and regional impacts in the winter season are described in section 3. In the last Section, we summarized our results.

2. Material and Methods

2.1 Model Description

To study global and regional climate responses caused by ENSO forcing, we employed a Geophysical Fluid Dynamics Laboratory global High-Resolution Atmospheric Model (GFDL-HiRAM) effectively at 25 km horizontal grid resolution. The HiRAM model uses a cubed-sphere finite-volume dynamical core that is based on GFDL's Atmospheric Model version 2 (AM2; *Putman and Lin, 2007*; *Anderson et al., 2004*) with increased horizontal and vertical resolutions (32 vertical layers instead of 24 for better representation of stratospheric processes and its coupling with the troposphere), as well as simplified parameterizations for moist convection and large-scale stratiform cloudiness. HiRAM uses a new grid-point dynamical core along with a prognostic cloud scheme, multi-species aerosol climatology as well as components from previous models used at GFDL. However model retains the surface flux, land surface, gravity wave drag, boundary layer, radiative transfer modules, and large-scale cloud microphysics of AM2 *(Anderson et al. 2004; Zhao et al. 2009)*. Soil processes considered in HiRAM are calculated using a land model known as LM3 that includes soil sensible and latent heat storage, groundwater storage, and stomata resistance (*Anderson et al., 2004*).

The shortwave (SW) radiation processes are calculated using Freidenreich and Ramaswamy (1999) algorithm. The SW radiation spectrum ranges from 0.17 to 4.0 µm, which is divided into 25 bands, 10 in the near IR region, 4 bands in the visible and 11 bands in the UV region and includes absorption by H_2O, CO_2, O_3, O_2 as well as Rayleigh scattering. The longwave (LW) radiation code is based on a modified form of the simplified exchange approximation (*Schwarzkopf and Ramaswamy, 1999*). It accounts for the absorption and emission by the principal gases present in the atmosphere including H_2O, O_3, CO_2, N_2O, CH_4, and the halocarbons CFC-11, CFC-12, CFC-113, and HCFC-22. Aerosols and clouds are treated as absorbers in the longwave, with non-grey absorption coefficients specified in the eight spectral bands of the transfer scheme, following the methodology adopted in Ramachandran et al. (2000). A detailed description of the HiRAM model and related publications is available at http://www.gfdl.noaa.gov/HiRAM.

2.2 Experimental Design and Methodology

In this study, we used HiRAM simulations at C360 (~25 km) horizontal resolution, typically a range that most of the regional climate models (RCMs) use in climate downscaling. This allows us to study global and regional climatic processes using a global climate model (GCM) that fully accounts for regional and global scale interactions, which are especially important in the tropics. The model is forced with observed monthly SST from the Hadley Centre Sea Ice and Sea Surface Temperature (HadISST) data set (*Rayner et al., 2003*). Three parallel simulations each of 33 years simulation period (1976-2008) are conducted by taking into account greenhouse gases and volcanic forcing. The aerosol spatial time distribution and optical characteristics of volcanic aerosols (that were released by the volcanic eruption events in the simulation period) are calculated following Stenchikov et al. (2006). To reduce the uncertainty (due to internal noise) in the model results, an ensemble averaging over three HiRAM realizations is used. These three realizations were produced using different initial conditions obtained from several integrations of the atmosphere-only model. The first realization uses SST of Jan 1976, whereas second and third realizations use Jan 1977 and Jan 1978 respectively from HadISST. In order to avoid spin-up effects, first three years of the integration (1976-1978) in each realization are not included in the analysis. Model is run in Atmospheric Model Inter-comparison Project (AMIP) mode with observed SST and sea ice concentration determined from the HadISST data set. The sea-ice model assumes that each grid-point is either fully ice-covered or ice-free and also considers a uniform ice thickness of 2 meters.

Anthropogenic greenhouse gases (GHGs), natural forcings, ozone, landuse and other possible forcings data set (anthropogenic aerosols concentration in the atmosphere etc.) used in the model follows AMIP historical simulation setup.

For comparison of the HiRAM response, we used NCEP-climate forecast system reanalysis (CFSR) data. CFSR is a high-resolution reanalysis data produced using NCEP coupled atmosphere-ocean-land surface-sea ice model (coupled with GFDL MOM version 4 and a two-layer sea ice model). Most of the available in-situ and satellite observations are included in the CFSR. Satellite observations are used in form of radiance, rather than retrieved values, and are bias-corrected with "spin up" runs at full resolution. It is a recent NCEP reanalysis data that assimilates surface observations, satellite radiances, CO_2, aerosols (including volcanic aerosols), and solar variations using a high-resolution atmospheric model at T382 (~38 km) horizontal resolution with 64 vertical levels ranging from the surface to 0.26 hPa. Annual averages of time-varying CO_2 concentration including other radiatively absorbing gases; stratospheric volcanic aerosols and downward solar radiation flux in CFSR are specified as described in Saha et al. (2010).

The ocean effect is included as we used observed SST that takes into account the ocean feedback. It is not interactive, but it allows us to correctly account for such an aspect of natural variability as El Niño. Typically, coupled models could have a problem in correctly reproducing the phase and magnitude of the ENSO, so in this case we have an "ideal" observed SST forcing. Using atmospheric model with the prescribed SST is, of course, an idealized approach, but fairly reasonable one, as demonstrated in previous studies (Stenchikov et al., 2002; Dogar et al., 2017b). The ocean effect in our simulations is not interactive but it is not absent. The observed SSTs, used in the calculations, account for the ocean effect. Thus, in our simulations the atmospheric response is fully interactive, and is constrained by observed ocean boundary conditions. This approach allows us to more reliably evaluate the contributions of different processes and compare our results with observations.

For strong El Niño episodes, we composited all the winter (DJF) seasons during the period 1979-2008 that have SST anomaly equal or greater than 1.5 K over the Nino3.4 region. Whereas for the case of weak El Niño, we composited all the winter seasons with SST anomaly with magnitude 0.5 to 1.5 K. For the case of La Niña, a same approach is applied, however, the SST anomaly values over the Nino3.4 region is negative. For details regarding strong or weak ENSO episodes, the readers may visit the link https://ggweather.com/enso/oni.htm. As ENSO predominantly triggers/peaks in winter, therefore, we have presented anomalous signals for strong and weak ENSO episodes in boreal winter (DJF) season only. The impact of stronger and weaker ENSO magnitude is calculated as a simple departure of the stronger and weaker El Niño and La Niña composited averages from the long-term winter (DJF) climatology that includes all the El Niño and La Niña events in the simulation period (1979-2008) and roughly corresponds to neutral phase. The HiRAM simulation results are compared with a high-resolution CFS Reanalysis (CFSR) product.

3. Results and Discussion

Before examining the impacts of strong and weak ENSO forcing at the global and regional scale, we assessed the performance of HiRAM AGCM. Figure 1 shows the climatology pattern of 2m surface temperature and rainfall superimposed with wind vectors produced using CFSR and HiRAM model. These climatology maps clearly show that HiRAM model reproduces both qualitatively and quantitatively the basic features of temperature and precipitation very well. The convergence zones and cyclonic flow patterns in the Northern Hemisphere shown by zonal and meridional wind vectors are well captured by the model simulation. This comparison increased our confidence in the HiRAM simulation that motivated us to use this model for the assessment of ENSO magnitude at the global and regional scale. Therefore, to have a better representation of the ENSO-induced teleconnection patterns, we analyzed anomalous atmospheric responses following the El Niño and La Niña events composited over the period of 1979-2008 (see methodology), as discussed in the following sections.

3.1 Strong ENSO Winter Impacts

Figure 2 shows the global anomalous response of surface temperature at 2m following strong El Niño and La Niña forcing in CFSR and HiRAM. Both the HiRAM and CFSR results show strong warming over the eastern part of the tropical Pacific extending towards North America (Eastern and Central America) as well as over Eurasia with strong cooling anomalies in the western Pacific Ocean as well as over the Arctic Ocean. This El Niño-induced warming pattern seen in the tropical Eastern Pacific extending further into North Pacific and Central American region resembles a well-known horseshoe-like warming pattern. We also observed strong warming over parts of Southwestern Europe, Southern Africa, the Indian Ocean, and Australia. We noticed that the model well reproduced the observed features at the global scale with slight underestimation of the cooling signal over the Arctic region as well as the Arabian Peninsula and North Africa. This underestimation could be accounted for due to HiRAM weak response to ENSO-induced stratospheric polar vortex variation (i.e., weakening or strengthening) following El Nino/La Nina events and associated NAO-like pattern. The stratospheric polar vortex and associated NAO-like response are underestimated in HiRAM, like other global models, and therefore the associated temperature (i.e., cooling) response following El Nino in the high-latitude (i.e., mid-latitude and polar regions) is underestimated in HiRAM compared to CFSR. Polar vortex is a stratospheric phenomenon that is transported to surface through tropospheric–stratospheric interactions. These polar vortex changes (strengthening or weakening) following ENSO events effects polar jets that in turn produce strong changes in the mid-latitude and polar regions. HiRAM has a lower model top (that covers lower stratosphere, model top reaches 10 hPa) compared to CFSR (that covers entire stratosphere, model top reaches 0.1 hPa), which could be one of the reason that the HiRAM underestimates weakening (i.e., breakdown) or strengthening of polar vortex and associated circulation changes following internal or external climate forcing (Dogar, 2018; DallaSanta et al., 2019; Marathe & Karumuri, 2021; Dogar, 2019). Further discussion regarding HiRAM underestimation to ENSO forcing can be seen in supplementary Fig. S1 and S2. A reverse anomalous pattern is roughly observed following strong La Niña episode both in the HiRAM and NCEP-CFSR except over the Arabian Peninsula as well as over North America and Eurasia where the cooling or warming signals are not anti-symmetric following strong El Niño and La Nina episodes. This ENSO-induced (El Niño/La Niña) tropical warming/cooling pattern outspreading to the Arctic and North American region is caused by a well-known ENSO-induced tropically excited Arctic warming/cooling mechanism following the strong El Niño/La Niña events. In this tropically excited Arctic mechanism, the pole-ward propagating Rossby waves can warm/cool the Arctic region through adiabatic warming/cooling mechanism, an enhanced pole-ward stationary eddy heat transport, and downward infrared radiation (Saravanan, 1993; Lee et al. 2012).

We also noticed a strong El Niño/La Niña-induced cooling/warming pattern over Northern/Southern Africa that could be accounted for by large-scale dynamic circulation and associated diabatic processes driven by Walker circulation and its transport from the tropics towards extratropics through the latitudinal thermal gradient. Another mechanism of this African continental cooling/heating could be explicated through convectively generated Rossby waves. These waves emanate from the equatorial Pacific, moving eastward in circular paths resulting in wind and pressure changes that play a key role in the transport of heating or cooling anomalies in the tropics and outside the tropics (Jin and Hoskin 1995; Servan, 1993; Kiladis et al. 2009; Lee, 2012). Temperature anomalies induced by strong El Niño forcing are very much consistent between the model and CFSR. The anomalous 2m-temperature response following the La Niña forcing is roughly opposite to the El Niño forcing. It suggests that the La Niña forcing will induce stronger cooling over North America, Europe, Arabian Peninsula, and the African domain. From the spatial anomaly pattern of surface temperature at 2m, we noticed that the HiRAM model reproduces the impact of ENSO over the Pacific, North and South America very well and our results are consistent with earlier studies (Sterl et al. 2007; Lee, 2012; Wang et al. 2012). However, it underestimates ENSO teleconnection pattern and associated changes over the Middle East and North Africa particularly over the Arabian Peninsula region, covering the Red Sea which could be accounted for by the variations of ENSO-induced circulation changes (e.g., PNA and NAO) that could not be well reproduced by the model as it has been noticed that the HiRAM model, like other up-to-date climate models, underestimates the response of NAO in winter (Dogar, et al., 2017b; Driscoll et al., 2012).

Figure 3 shows the response of precipitation in winter season following strong El Niño and La Niña events. The pattern of precipitation anomaly following both the El Niño and La Niña shows a stronger signal over the tropics compared to extratropics. The spatial pattern of precipitation anomaly (mm/d) reveals that El Niño forcing causes an increase in precipitation over the east and central equatorial Pacific region and a decrease in precipitation in the western Pacific. This is consistent with the warm anomaly in the east and central equatorial Pacific and cold anomalous signal in the western Pacific Ocean, respectively, as observed in the 2m-temperature pattern (Figure 2). These warm (cold) surface features produce more (less) moisture transport that result in increased (decreased) rainfall anomalies over the equatorial regions. We find that the strong El Niño (La Niña) forcing typically reduce (intensifies) precipitation over the southern Africa in particular southeastern region, resulting in dry (wet) conditions, while increasing (reducing) precipitation over the northeastern tropical region.

We also noticed that El Niño-induced warm anomaly over the tropics causes more precipitation over the ascending branch (i.e., ITCZ) of the Hadley cell. Subtropical regions that fall within the downward or sinking branch of Hadley cell exhibit reduced precipitation anomalies which are very much in agreement among CFSR and HiRAM. Since the latitudinal position of the rising and sinking limbs of local Hadley cell varies at the regional scale, therefore increasing and decreasing pattern of precipitation anomalies over the tropical region corresponds to the position of the ITCZ at the regional scale.

A positive precipitation anomaly and cyclonic circulation response are seen near the California coast and Aleutian region as well as in the Gulf of Mexico, Cuba, and Florida region, extending further into the western Atlantic. El Niño also causes a decrease in precipitation over Bay of Bengal, Sri Lanka, Thailand, Australia, and Columbia. This ENSO-induced winter precipitation anomaly for the El Niño forcing is consistent with earlier studies showing a comparison of precipitation anomaly between NCEP reanalysis and SPEEDY AGCM by regressing the normalized Nino3.4 index with winter precipitation (Sterl et al. 2007; Kucharski et al. 2013). The overall pattern of ENSO-induced precipitation changes over global and regional scale is well reflected in HiRAM simulation and is in good agreement with CFSR and earlier studies (Dogar et al., 2017a; Kucharski et al., 2013). Precipitation anomalies for La Niña conditions are roughly opposite to that of El Niño. A dipole pattern of precipitation anomalies in high-latitudes (between 30-60°N and 30-60°S) following both El Niño and La Niña forcing could be associated with the ascending and descending branch of the Ferrell cell.

In order to have a better idea of ENSO-induced changes in the tropical Hadley circulation, we have plotted vertical velocity (Omega in Pa/sec) overlaid with ascending and descending air produced by globally zonal averaged meridional and vertical wind profile (Fig. 4). These results suggest that both the El Niño and La Niña induce strong impact over the tropical atmospheric Hadley circulation as both the vertical velocity and the intensity of the wind vectors have increased significantly following strong El Niño event. We further noticed that strong El Niño forcing induces strengthening and equatorward shift to Hadley cell (sinking limbs are stronger and confined within 10-25° latitude in both hemisphere) whereas the La Niña causes weakening to the Hadley cell circulation. The structure of zonally averaged zonal wind anomaly following El Niño and La Niña episode in winter season shows that the El Niño produces strengthening and equatorward shifting to the jet streams (not shown). This ENSO-induced strengthening and equatorward shift of jet streams leads to a narrower but intense Hadley cell circulation (Figure 4) because of increased eddy stress (Lee, 2012). The response of Hadley cell to La Niña forcing is almost opposite to El Niño forcing. Figure 5 presents ENSO-induced changes in tropical Walker circulation which shows consistent pattern of rising and sinking limbs between CFSR and HiRAM. These El Niño-induced rising patterns of the wind vectors over the tropical Pacific and the tropical Indian Ocean match with El Niño-induced sea surface temperature (SST) warming in the tropical Pacific and the tropical Indian Ocean (Figure 2). This ENSO-induced perturbation of the Walker circulation causes major shifts in atmospheric circulations, rainfall patterns, and seasonal climate around the globe.

Figure 6 shows the response of geopotential height anomaly at 850 hPa following strong El Niño and La Niña phases from HiRAM and NCEP-CFSR in winter (DJF) season. During strong El Niño forcing geopotential height at 850 hPa shows a strong negative anomaly over the high-latitude region (between 30-60N) in the Pacific Ocean extending towards the Atlantic ocean and a signature of high anomalies over rest of the tropical belt particularly over the Indian Ocean focusing the Arabian Sea that extends further to land areas of Africa, South, and Southeast Asia (Sterl et al., 2007). Similarly, we observed signature of negative anomalies in high-latitude northern polar regions and positive anomalies in the Southern Ocean. The anomaly of significant high and low pressure further elongates zonally to the Atlantic Ocean and resembles a positive NAO-like anomalous pattern over the Atlantic Ocean (Zhang et al. 2015). This positive NAO-like pattern will produce a significant impact over Northern and Southern Europe extending to the Middle East and North African region and induces cold and wet anomalies as seen in 2m surface temperature and precipitation (Fig. 2 and Fig. 3 respectively) patterns (Shindel et al. 2004; Yu and Zhou, 2004; Fischer et al. 2007). The mechanism that could explain this positive NAO-like pattern and associated effects over Europe focusing southern Europe, Arabian Peninsula and North African domain is caused by the convectively generated coupled Rossby waves (Saravanan, 1993; Jin and Hoskins, 1995; Kiladis et al. 2009; Lee, 2012). The La Niña phase also displays a positive NAO-like pattern over the North Atlantic region that will also result in cooling and drying anomalies over Southern Europe and MENA region. Interestingly, the ENSO-induced NAO-like response over the North Atlantic Ocean is more pronounced in the CFSR results than in HiRAM therefore associated changes over Europe and MENA are also slightly underestimated in HiRAM response. These results reveal that the climatic impacts of ENSO over the global and regional scale are very sensitive to the intensity of ENSO and its warming and cooling phase in the tropical Pacific Ocean. The geopotential height response and associated climatic patterns in the North Pacific are caused as a result of a well-known boreal winter ENSO teleconnection pattern induced by the Rossby wave source in the tropics that propagates towards extra-tropics and forms a quasi barotropic structure. This wave train effect projects onto the Pacific North American (PNA) pattern, and the Aleutian low. This prominent teleconnection associated with ENSO (El Niño/La Niña) events has been referred to as the PNA pattern accompanied by an intensified Aleutian low during ENSO warm (El Niño) phase. Corresponding to the ENSO (La Niña) cold phase, a positive geopotential height anomaly covers the North Pacific indicating a weakened Aleutian Low during the La Niña events. This type of pattern is anticipated to induce energy transport among tropics, extra-tropics and high-latitude regions following El Niño and La Niña forcing (Lee, 2012). Figure 7 shows the pattern of geopotential height anomaly at 200 hPa following strong El Niño and La Niña forcing. This upper level geopotential height anomaly is high in the tropics and low in the subtropical region because the positive ENSO phase (El Niño) overall warms the tropical atmosphere. This leads to high geopotential height anomalies at the upper levels as a result of hydrostatic equilibrium. The geopotential height is lower in the more northern latitudes because of wave propagations of various types. This upper-level geopotential height anomaly is stronger over the tropical Pacific Ocean compared to the rest of the tropical regions, which is associated with the El Niño-induced strong tropical Pacific warming pattern. These results are qualitatively consistent with observational, reanalysis and model based studies showing Nino3.4 regressed anomalous pattern of geopotential height changes (Sterl et al. 2007; Kucharski et al. 2013; Dogar et al., 2017a). Responses of geopotential height anomalies following strong La Niña episodes display a mirror image to their El Niño counterparts.

3.2 Weak ENSO Winter Impacts

Figure 8 shows the global anomalous response of 2m surface temperature following weak El Niño and La Niña forcing in CFSR and HiRAM. Both the HiRAM and CFSR results show strong warming over the tropical eastern Pacific extending towards North America (Eastern and Central America) as well as over Eurasia with weak cooling signatures in the Western Pacific and Arctic Oceans. We also noticed a strong warming pattern over parts of South Western Europe, Africa, the Indian Ocean, and Australia. Model is reproducing the observed features very well at the global scale with underestimation of the cooling signal over Eurasia. A circumpolar westerly jet, confining the coldest temperatures over the Arctic, characterizes the wintertime stratospheric polar vortex. This underestimation could be accounted for by the strength of ENSO-induced stratospheric polar vortex and associated circulation changes (supplementary Figs. S1 and S2). The stratospheric polar vortex in winter and associated tropospheric and surface circulations (e.g., polar jets and NAO-like response at surface) are underestimated in HiRAM, and therefore the warming/cooling response following weak El Nino/La Nina in the Eurasian region is not well captured by HiRAM compared to CFSR. We also observed differences over northern Europe and the northern part of Eurasia where the HiRAM model shows strong cooling compared to CFSR, which shows warming. A reverse anomalous pattern is roughly observed following weak La Niña episode both in the model and NCEP-CFSR except the Eurasian region where we saw strong warming in Model results and cooling response in CFSR. Moreover, the cooling signal over the North American region following weak La Niña is stronger in the CFSR results whereas it is weaker in the HiRAM results. These results suggest that the HiRAM model struggles in reproducing the teleconnection response for weaker ENSO, especially over Eurasia, parts of the Arabian Peninsula, and America. This ENSO (El Niño/La Niña)-induced tropical warming/cooling pattern extending to the Arctic and North American region is caused by a well-known ENSO-induced tropically excited Arctic warming/cooling mechanism following the El Niño/La Niña forcing. In this tropically excited Arctic mechanism, the pole-ward propagating Rossby waves can warm/cool the Arctic through adiabatic warming/cooling mechanism, an enhanced pole-ward stationary eddy heat transport, and downward infrared radiation (Saravanan, 1993; Lee et al., 2012). We noticed that the La Niña forcing induces a stronger cooling over the tropical central Pacific that propagates to North America, Europe, Arabian Peninsula, and South Africa. From the spatial anomaly pattern of 2m surface temperature, we noticed that the HiRAM model reproduces the impact of ENSO over the Pacific, North and South America reasonably well and simulated results are in agreement with earlier studies (Lee, 2012; Wang et al., 2012; Sterl et al., 2007), however, it underestimates and gives feeble responses to weak ENSO teleconnection pattern and associated changes over the Indian subcontinent, Eurasia, parts of Southern Europe, Northern and Central America, parts of Arabian Peninsula including the Red Sea, which could be accounted for by the variations in stratospheric and tropospheric aerosol impact caused by two major eruptions falling in the simulation period during ENSO events. It could also be attributed to ENSO-induced circulation changes (e.g., NAO) that like other models are not well reproduced by HiRAM (Driscoll et al., 2012; Dogar et al., 2017b).

Figure 9 shows the response of precipitation anomaly (mm/d) in the winter season following weak El Niño and La Niña events. The pattern of precipitation anomaly following both El Niño and La Niña shows a stronger signal over the tropics compared to extratropics. The spatial pattern of precipitation anomaly indicates that El Niño forcing is causing an increase in precipitation over the east and central equatorial pacific region and decreased precipitation in the western pacific. This is consistent with the warm anomalous pattern in the east and central equatorial Pacific and cold anomalous pattern in the western equatorial Pacific respectively as observed in 2-m surface temperature pattern (Figure 8). These warm (cold) surface features cause more (less) moisture convergence, resulting in increased (decreased) rainfall anomalies over the equatorial regions. We also noticed that El Niño induced warm anomaly over the tropics causes more precipitation over the upward branch (i.e., ITCZ) of the Hadley cell. Subtropical regions that fall within the descending or sinking branch of Hadley cell display reduced precipitation anomalies which are very much in agreement among CFSR and HiRAM. As the latitudinal position of the ascending and descending limbs of local Hadley cell varies at the regional scale (Schwendike, 2014), therefore, the increase and decrease in precipitation anomalies over the tropical region follow the position of ITCZ at the regional scale. The overall pattern of precipitation changes caused by ENSO on the global and regional scale is well reflected in HiRAM simulation, and it is in good agreement with CFSR and earlier studies (Kucharski et al. 2013). The precipitation anomalies obtained for La Niña conditions are roughly opposite to El Niño impact, however, we noticed some differences in the model responses especially following weak La Niña that could be accounted for by model underestimation to circulation changes (Dogar and Sato, 2018; 2019).

To have a better idea of weak ENSO-induced changes in the tropical Hadley circulation, the vertical velocity (Omega in Pa/sec) overlaid with rising and sinking air produced by globally zonal averaged meridional and vertical wind profile are plotted (Fig. 10). These results reveal that, similar to strong ENSO, both the weak El Niño and La Niña also induce a strong impact on the Hadley circulation as both the vertical velocity and the intensity of the wind vectors have increased significantly following the weak El Niño event. We further find that the El Niño induces strengthening and equatorward shift of Hadley cell (i.e., sinking limbs are strong and confined within 10-25° latitude in both hemispheres) whereas La Niña causes a reverse pattern. Although the model well captures the rising and sinking branches of the Hadley cell, nevertheless the intensity is much weaker in the model response compared to the CFSR. The pattern of zonally averaged zonal wind anomaly following El Niño and La Niña episodes in the winter season shows that the El Niño forcing produces strengthening and equatorward shift to the jet streams (not shown). This ENSO-induced strengthening and shift of jet streams towards equator result in a narrower but intense Hadley cell (Figure 4) because of increased eddy stress. The results of Hadley cell response to La Niña are almost opposite to El Niño forcing. Figure 11 presents ENSO-induced changes in tropical Walker circulation, which show a consistent pattern of rising and sinking limbs between CFSR and HiRAM. However, the intensity of the model response is much weaker compared to CFSR and there also exist some variations such that the model shows a rising pattern at 60°W while the reanalysis shows a mixed pattern.

Figure 12 shows the response of geopotential height (GH) anomaly at 850 hPa following weak El Niño and La Niña phases from HiRAM and NCEP-CFSR in the winter season. The geopotential height at 850 hPa following weak El Niño forcing shows a negative anomaly structure over the high-latitude region (between 30-60°N) in the Pacific and North Atlantic Oceans. A signature of positive anomalies is seen over the tropical belt particularly over the Indian Ocean focusing the Arabian Sea that extends further to land areas such as Australia, Africa, South Asia, and Southeast Asia (Sterl et al. 2007). Similarly, we observed negative anomaly signature in the Arctic region and slight positive anomaly signature in the Antarctic region (especially in the HiRAM response) following the weak El Niño. The anomaly of high and low pressure over the Pacific region elongates zonally to the Atlantic Ocean and resembles a positive NAO-like pattern over the Atlantic Ocean (Zhang et al. 2015). However, the magnitude of this geopotential height anomaly is weak following weak ENSO forcing. This positive NAO-like pattern produces significant impacts over Northern and Southern Europe, extending to the MENA region, with cold and wet anomalies as seen in 2m surface temperature and precipitation (Fig. 8 and Fig. 9 respectively). However, the magnitude of these responses is much weaker. This NAO-like pattern and associated effects over Europe focusing southern Europe, Arabian Peninsula, and North African domain is caused by convectively generated coupled Rossby waves (Lee, 2012; Jin and Hoskins, 1995; Kiladis et al. 2009). The La Niña phase also exhibits a positive NAO-like pattern in the North Atlantic region, leading to cooling and drying anomalies in Southern Europe and MENA region. Nevertheless, HIRAM does not well capture this NAO-like response and gives different pattern following weak La Niña event. As explained earlier, the ENSO-induced geopotential structure that resembles NAO-like response over the North Atlantic Ocean is more pronounced in CFSR than HiRAM, so the associated changes over Europe and MENA are also slightly underestimated in the HiRAM response. Moreover, the responses both following El Niño and La Niña are somehow varying between HiRAM and CFSR. These results suggest that the climatic impacts of ENSO on the global and regional scales are very sensitive to the intensity of ENSO in the tropical Pacific. The geopotential height response in the North Pacific is caused as a result of a well-known winter ENSO teleconnection pattern induced by the Rossby wave source in the tropics that propagates towards extra-tropics and forms a quasi barotropic structure. This wave train effect is weaker following weak ENSO episodes. Therefore, the PNA and NAO-like structures observed after strong ENSO episodes are not much obvious after weak ENSO episodes. Figure 13 shows the pattern of geopotential height at 200 hPa following weak El Niño and La Niña forcing. The response of geopotential anomaly at the tropical Pacific region resembles the Matsuno-Gill type pattern in the tropical Central Pacific (Gill, 1980). However, its magnitude following weak ENSO forcing is weaker than strong ENSO forcing. This upper-level geopotential height anomaly following El Niño/La Niña is high/low in the tropics and low/high in the subtropics because the positive/negative ENSO phase overall warms/cools the tropical atmosphere. This leads to high/low geopotential anomalies in the upper levels as a result of hydrostatic equilibrium. The height is lower in the more northern latitudes because of wave propagations of various types. This upper-level geopotential height anomaly is stronger over the tropical Pacific compared to the rest of the tropics, which is associated with the El Niño-induced tropical Pacific warming pattern. These results are qualitatively consistent with earlier observational and modeling studies showing Nino3.4 regressed anomalous pattern of geopotential height changes (Dogar et al., 2017a; Kucharski et al. 2013; Sterl et al. 2007). We noticed that the response of the geopotential height anomaly following the La Niña episode does not reflect a reverse pattern over the tropics or extratropics. Moreover, the response of model is also not very similar to CFSR over high-latitude regions in both hemispheres, especially in the Arctic and Antarctic areas.

3.3 Response of MENA and Asia to Strong and Weak ENSO

To better highlight model response regional climate response of the HiRAM model to strong and weak ENSO forcing, we looked at the response of 2m surface temperature and precipitation over the MENA regions. We focused on the MENA and Asia, as these regions are among the most sensitive regions and several studies previously used HiRAM model to better understand the climate of these regions (Bangalath and Stenchikov, 2015; Dogar et al., 2017b; Dogar and Sato, 2018; 2019). Figure 14 shows the case of strong ENSO forcing over the MENA and Asian region. ENSO-induced warming over Northern Europe, Russia, and the tropical Indian Ocean region and cooling over Africa, the Middle East, and the Asian region is consistent among the reanalysis and HiRAM. However, we noticed this warming and cooling structure is more pronounced in the reanalysis compared to the model that could be associated with the global climate model's weak response to ENSO-induced circulation changes (Dogar et al., 2017b; Dogar and Sato, 2018; 2019; Robock, 2012; Timmreck 2012). The warming and cooling anomaly following strong La Niña is also somehow consistent between the model and the reanalysis except for Central Africa, and India where there appeared a different anomalous structure that could be associated to model weak response to ENSO-induced circulation changes such as ENSO-induced NAO-like response. Figure 15 shows the precipitation changes over the MENA region following strong El Niño and La Niña forcing. The strong El Niño forcing causes enhanced precipitation over the Arabian Sea and decreased precipitation over the Bay of Bengal. The structure of precipitation response is largely consistent between the HiRAM and the CFS reanalysis. However, there exists slight variation over the Indian Ocean following the La Niña forcing. Moreover, we noticed that the response of weak ENSO forcing on the MENA region is much different and the HiRAM model gives a different structure of 2-m surface air temperature over Europe and the Eurasian region (Figure 16), suggesting that the weak ENSO forcing response is not well reproduced by HiARM model over the MENA and Asia. The structure of precipitation response, especially over Europe, India including the Arabian Sea is also different between the model and the reanalysis following weak La Niña forcing in the winter season (Figure 17). Supplementary Figures S1 and S2 and associated discussion regarding HiRAM response to circulation changes could account for discrepancies/biases between HiRAM and CFSR. This supplementary analysis highlights the importance/need of air-sea coupling (for better simulation of ENSO-induced thermal changes) and enhanced model top (to better account for stratospheric processes, e.g., polar vortex changes and NAO-like teleconnection). Therefore, systematic improvements in GCMs are needed to better simulate ENSO-induced circulation changes and associated climatic impacts especially for MENA region, which being part of the Hadley cell, is sensitive to internal and external climate drivers (e.g., aerosol forcing or internal variability). Due to low model top, vertical variations of stratospheric dynamics and the impact of the stratospheric polar vortex are underestimated in HiRAM. Hence, by considering air-sea coupling and increased model top in high-resolution AMIP-type simulations could improve the biases between the observations and simulation following strong and weak ENSO forcing.

4. Summary and Conclusions

The present study is an attempt to evaluate the role of ENSO intensity (i.e., strong and weak El Niño/La Niña) in causing global and regional climate changes using a very high-resolution atmospheric model (HiRAM), effectively at 25 km grid spacing. HiRAM simulated responses to ENSO strength using 2m surface temperature, precipitation, geopotential height and vertical wind composited anomaly pattern following El Nino/La Nina during the period 1979-2008 are compared with a high-resolution CFS reanalysis, which is available at 38 km grid spacing.

Earlier studies suggest that the intensity and frequency of ENSO events have increased over the last few decades resulting in a need to study the global and regional climatic impacts of ENSO strength. Although, the main progress on the study of ENSO events and their climatic impacts was initially made using climate models of intermediate complexity. However, these intermediate complexity models have a coarse resolution, limiting them to have a detailed analysis of ENSO-induced climatic responses, especially at the regional scale. Hence, to better understand ENSO-induced climatic impacts at the global to regional scale, we used a high-resolution atmospheric model, HiRAM, developed at GFDL, effectively at 25 km grid resolution. We have analyzed the impact of El Niño/La Niña magnitude on 2m surface temperature, precipitation, sea level pressure, vertical wind, and geopotential height at the global and regional scale focusing on the tropical and extratropical regions.

The results obtained using HiRAM atmospheric model show that ENSO has a stronger impact over the Inter-tropical Convergence Zone (ITCZ) region compared to extratropics and high-latitude regions. These results are largely consistent with the findings of Zhao et al. (2016) who showed that the ocean forcing from the ENSO is secondary and tend to be confined in the tropics. However, the study of Zhao et al., 2016 did not categorize ENSO into strong and weak ENSO events. We further noticed that the strong ENSO positive phase causes a significant weakening of rainfall over Africa, South Asia whereas the La Niña phase of strong ENSO produces more rain over these regions. The model results also reveal that ENSO has a stronger impact over South Asia particularly over the Indian region because of its significant impact over the Indian Ocean focusing on the Arabian Sea, the Bay of Bengal, and the Laccadive Sea through the Walker circulation.

Analysis of precipitation anomalies, zonal-mean vertical wind, and geopotential height changes at 850 and 200 hPa, reveal that the ENSO magnitude significantly impacts Hadley and Walker circulation. Model-based configuration of Hadley cell following strong and weak El Niño (La Niña) events emphasizes that the intensity of Hadley rising and sinking branches increased (decreased) significantly exhibiting that Hadley circulation is very sensitive to the magnitude of ENSO forcing. ENSO-induced changes in precipitation and vertical wind profile suggest that strong ENSO positive phase (El Niño) can induce strengthening and equatorward shrinking to Hadley cell whereas the negative phase of strong ENSO (La Niña) causes weakening of tropical Hadley cell. These AMIP-style HIRAM-based ENSO experiments further reveal that the strong El Niño (La Niña) induces significant weakening (strengthening) to local Hadley cell covering MENA and Asian tropical regions, which may cause weakening (strengthening) of Indian and African rainfall, indicating that MENA and South Asian tropical regions are very sensitive to tropically excited SST changes. This ENSO-induced strengthening and weakening of Hadley cell along with variations in Walker circulation induce significant impact over tropical regions covering South and Southeast Asian and African rain-belt regions. Our study reveals that strong El Niño (La Niña) episodes cause strengthening (weakening) and equatorward (poleward) shift to jet streams.

Analysis of geopotential height (GH) changes suggests that ENSO-induced negative (positive) NAO-like response and associated changes in Southern Europe and MENA region become significantly strong following the increased intensity of El Niño (La Niña) in the northern hemisphere in the boreal winter season. The HiRAM model reproduces the impact of ENSO over the Pacific, North and South America, and African region quite well however it fails to accurately produce ENSO teleconnection patterns and associated changes in temperature and precipitation following weak ENSO events. One of the possible reasons for this disparity could be that the ENSO-induced NAO-like response might be a key component that is not well reproduced by the model.

Our study suggests that ENSO-induced changes in sea surface temperature over the tropical Indian Ocean could play a significant role in governing teleconnections through changes in Walker circulation that consequently induces changes in the meridional thermal gradient. This study further concludes that SST forcing in the tropical Indian and the Pacific Ocean and their teleconnection through large-scale zonal atmospheric overturning circulation is attributed to be a potentially important driving condition for fully characterizing ENSO-induced climatic changes in South Asia. In general ENSO-induced global and regional teleconnection patterns of surface temperature, precipitation, sea level pressure (SLP) and geopotential height changes are consistent with CFSR as well as with earlier studies, which indicates that the HiRAM model can be used effectively to better understand ENSO-induced global and regional climatic responses.

The HiRAM model underestimated the cooling response following strong ENSO over the MENA region that could be accounted for by HiRAM weak response to ENSO-induced NAO-like teleconnection and associated regional impacts over MENA. We further find that the HIRAM model well reproduced the Matsuno-Gill pattern and horseshoe-like pattern following strong ENSO, however, these patterns are poorly reproduced following the weak ENSO phase resulting in varying regional climatic impacts over the MENA, Eurasian, South, and Southeast Asian regions, suggesting that HiRAM based ENSO results are sensitive to ENSO strength. The use of the air-sea coupling and increased model top (to better reflect ENSO-induced polar vortex changes) in high-resolution AGCM simulations could improve these biases between observations and simulations following strong and weak ENSO events.

Acknowledgements

We would like to thank the editor and two anonymous reviewers whose constructive suggestions and comments significantly improved the manuscript. An updated description of the latest version of the model used in this study as well as previous model versions is available at https://www.gfdl.noaa.gov/atmospheric-model/.

References

1. Afzaal M, Li JP, Jin FF (2013). The asymmetric influence of the two types of El Niño and La Niña on summer rainfall over Southeast China. J Clim 26:4567–4582.

2. Ashok, K., Guan, Z., & Yamagata, T. (2001). Impact of the Indian Ocean dipole on the relationship between the Indian monsoon rainfall and ENSO. Geophysical Research Letters, 28(23), 4499-4502.

3. Ashok, K., Guan, Z., Saji, N. H., & Yamagata, T. (2004). Individual and combined influences of ENSO and the Indian Ocean dipole on the Indian summer monsoon. Journal of Climate, 17(16), 3141-3155.

4. Ashok K, Behera S, Rao AS, Weng HY, Yamagata T (2007) El Niño Modoki and its possible teleconnection. J Geophys Res 112:C11007. doi:10.1029/2006JC003798.

5. Barimalala, R., A. Bracco, and F. Kucharski, 2011: The representation of the South Tropical Atlantic tele- connection to the Indian Ocean in the AR4 coupled models. Climate Dyn., doi:10.1007/s00382-011-1082-5.

6. Bhalme, H. N., & Mooley, D. A. (1980). Large-scale droughts/floods and monsoon circulation. Monthly Weather Review, 108(8), 1197-1211.

7. Bracco, A., Kucharski, F., Molteni, F., Hazeleger, W., & Severijns, C. (2007). A recipe for simulating the interannual variability of the Asian summer monsoon and its relation with ENSO. Climate dynamics, 28(5), 441-460.

8. Bulić, I. H., and Č. Branković (2007), ENSO forcing of the Northern Hemisphere climate in a large ensemble of model simulations based on a very long SST record, Climate dynamics, 28(2-3), 231-254.

9. Bulić, I. H., Branković, Č., & Kucharski, F. (2012). Winter ENSO teleconnections in a warmer climate. Climate dynamics, 38(7-8), 1593-1613.

10. Chung, C. T., Power, S. B., Arblaster, J. M., Rashid, H. A., & Roff, G. L. (2014). Nonlinear precipitation response to El Niño and global warming in the Indo-Pacific. *Climate Dynamics*, *42*(7-8), 1837-1856.

11. DallaSanta, K., Gerber, E. P., & Toohey, M. (2019). The circulation response to volcanic eruptions: The key roles of stratospheric warming and eddy interactions. *Journal of Climate*, *32*(4), 1101-1120.

12. Diaz, H. F., M. P. Hoerling, and J. K. Eischeid (2001), ENSO variability, teleconnections and climate change, International Journal of Climatology, 21(15), 1845-1862.

13. Dogar, M. M., Kucharski, F., & Azharuddin, S. (2017a). Study of the global and regional climatic impacts of ENSO magnitude using SPEEDY AGCM. Journal of Earth System Science, 126(2), 30.

14. Dogar, M. M., Stenchikov, G., Osipov, S., Wyman, B., & Zhao, M. (2017b). Sensitivity of the regional climate in the Middle East and North Africa to volcanic perturbations. Journal of Geophysical Research: Atmospheres, 122(15), 7922-7948.

15. Dogar, M. M., & Sato, T. (2018). Analysis of climate trends and leading modes of climate variability for MENA region. Journal of Geophysical Research: Atmospheres, 123(23), 13-074.

16. Dogar, M. M. (2018). Impact of tropical volcanic eruptions on Hadley circulation using a high-resolution AGCM.

17. Dogar, M. M. A. (2020). *Study of the regional climatic impacts of tropical explosive volcanism in the Middle East and North Africa region* (Doctoral dissertation, 北海道大学).

18. Dogar, M. M. (2019). The Sensitivity of DTR to the increased CO2 over Mid-latitude Semi-dry Regions.

19. Dogar, M. M., Kucharski, F., Sato, T., Mehmood, S., Ali, S., Gong, Z., ... & Arraut, J. (2019). Towards understanding the global and regional climatic impacts of Modoki magnitude. *Global and Planetary Change*, *172*, 223-241.

20. Dogar, M. M., & Sato, T. (2019). Regional climate response of Middle Eastern, African, and South Asian monsoon regions to explosive volcanism and ENSO forcing. *Journal of Geophysical Research: Atmospheres*, *124*(14), 7580-7598.

21. Dogar, M. M. A., & Shahid, A. (2018, December). Sensitivity of Hadley circulation to volcanic radiative forcing. In *AGU Fall Meeting Abstracts* (Vol. 2018, pp. A53M-2672).

22. Dogar, M. M. A., & Shahid, A. (2019, December). Revisiting the Climatic Impacts of ENSO Modoki Varying Magnitude. In *AGU Fall Meeting Abstracts* (Vol. 2019, pp. GC31D-1221).

23. Feng, J., and J. Li (2013), Contrasting impacts of two types of ENSO on the boreal spring Hadley circulation, Journal of Climate, 26(13), 4773-4789.

24. Fischer, E. M., J. Luterbacher, E. Zorita, S. F. B. Tett, C. Casty, and Wanner H. (2007), European climate response to tropical volcanic eruptions over the last half millennium, Geophysical Research Letters, 34(L05707), doi:10.1029/2006GL027992.

25. Frauen, C., Dommenget, D., Tyrrell, N., Rezny, M., & Wales, S. (2014). Analysis of the nonlinearity of El Niño–Southern Oscillation teleconnections. Journal of Climate, 27(16), 6225-6244.

26. Giannini, A., Biasutti, M., & Verstraete, M. M. (2008). A climate model-based review of drought in the Sahel: Desertification, the re-greening and climate change. Global and planetary Change, 64(3), 119-128.

27. Gill, A. E., (1980). Some simple solutions for heat-induced tropical circulation. *Quart. J. Roy. Meteor. Soc,* **106**, 447-462.

28. Held, I. M., & Hou, A. Y. (1980). Nonlinear axially symmetric circulations in a nearly inviscid atmosphere. Journal of the Atmospheric Sciences, 37(3), 515-533.

29. Hoerling, M. P., Kumar, A., & Zhong, M. (1997). El Niño, La Niña, and the nonlinearity of their teleconnections. *Journal of Climate*, *10*(8), 1769-1786.

30. Jin, F., & Hoskins, B. J. (1995). The direct response to tropical heating in a baroclinic atmosphere. Journal of the atmospheric sciences, 52(3), 307-319.

31. Ju, J., & Slingo, J. (1995). The Asian summer monsoon and ENSO. Quarterly Journal of the Royal Meteorological Society, 121(525), 1133-1168.

32. Kao, H. Y., & Yu, J. Y. (2009). Contrasting eastern-Pacific and central-Pacific types of ENSO. Journal of Climate, 22(3), 615-632.

33. Kiladis, G. N., Wheeler, M. C., Haertel, P. T., Straub, K. H., & Roundy, P. E. (2009). Convectively coupled equatorial waves. Reviews of Geophysics, 47(2).

34. Kug JS, Jin FF, An SI (2009) Two types of El Niño events: cold tongue El Niño and warm pool El Niño. J Clim 22:1499–1515.

35. Kripalani, R., Oh, J., Kulkarni, A. et al. Theor. Appl. Climatol. (2007) 90: 133. doi:10.1007/s00704-006-0282-0.

36. Kucharski, F., Molteni, F., & Bracco, A. (2006). Decadal interactions between the western tropical Pacific and the North Atlantic Oscillation. Climate dynamics, 26(1), 79-91.

37. Kucharski, F., Molteni, F., & Yoo, J. H. (2006). SST forcing of decadal Indian monsoon rainfall variability. Geophysical research letters, 33(3).

38. Kucharski, F., Bracco, A., Yoo, J. H., & Molteni, F. (2007). Low-frequency variability of the Indian monsoon-ENSO relationship and the tropical Atlantic: The "weakening" of the 1980s and 1990s. Journal of Climate, 20(16), 4255-4266.

39. Kucharski, F., Zeng, N., & Kalnay, E. (2013). A further assessment of vegetation feedback on decadal Sahel rainfall variability. Climate dynamics, 40(5-6), 1453-1466.

40. Kucharski, F., Molteni, F., King, M. P., Farneti, R., Kang, I. S., & Feudale, L. (2013). On the need of intermediate complexity general circulation models: a "SPEEDY" example. Bulletin of the American Meteorological Society, 94(1), 25-30.

41. Kumar, K.K., Rajagopalan, B., and Cane, M, A., 1999a: On the weakening relationship between the Indian monsoon and ENSO. Science, 284, 2156-2159.

42. Kumar, K.K., Kleeman R., Cane M. A., Rajagopalan B., 1999. Epochal changes in Indian monsoon-ENSO precursors. Geophys. Res. Lett. 26, 75.

43. Larkin NK, Harrison DE (2005). On the definition of El Niño and associated seasonal average U.S. weather anomalies. Geophys Res Lett 32:L13705. doi:10.1029/2005GL022738.

44. Latif, M., R. Kleeman, and C. Eckert (1997), Greenhouse warming, decadal variability, or El Niño? An attempt to understand the anomalous 1990s, J. Cl im., 10, 2221–2239, doi:10.1175 /1520-0442(19 97)010<2221: GWDVOE>2.0.CO;2.

45. Lean, J. L., & Rind, D. H. (2008). How natural and anthropogenic influences alter global and regional surface temperatures: 1889 to 2006. Geophysical Research Letters, 35(18).

46. Lee SK, Wang C, Enfield DB (2010) On the impact of central Pacific warming event on Atlantic tropical storm activity. Geophys Res Lett 37:L17702. doi:10.1029/2010GL044459

47. Lee, S. (2012). Testing of the tropically excited Arctic warming mechanism (TEAM) with traditional El Niño and La Niña. Journal of Climate, 25(12), 4015-4022.

48. Lau, N. C., & Nath, M. J. (2000). Impact of ENSO on the variability of the Asian-Australian monsoons as simulated in GCM experiments. Journal of Climate, 13(24), 4287-4309.

49. Lu, J., G. Chen, and D. M. W. Frierson, 2008: Response of the zonal mean atmospheric circulation to El Niño versus global warming. J. Climate, 21, 5836–5851.

50. Marathe, S., & Karumuri, A. (2021). The El Niño Modoki. In *Tropical and Extratropical Air-Sea Interactions* (pp. 93-114). Elsevier.

51.

52. Molteni F (2003) Atmospheric simulations using a GCM with simplified physical paraMeteorolrizations. I. Model climatology and variability in multi-decadal experiments. Clim Dyn 20:175–191.

53. Molteni F, Corti S, Ferranti L, Slingo JM (2003) Predictability experiments for the Asian summer monsoon: Impact of SST anomalies on interannual and intraseasonal variability. J Clim 16:4001–4021.

54. Molteni, F., King, M. P., Kucharski, F., & Straus, D. M. (2011). Planetary-scale variability in the northern winter and the impact of land–sea thermal contrast. Climate dynamics, 37(1-2), 151-170.

55. Nguyen, H., A. Evans, C. Lucas, I. Smith, and B. Timbal (2013), The Hadley circulation in reanalyses: Climatology, variability, and change, Journal of Climate, 26(10), 3357-3376.

56. Neelin, J. D., Battisti, D. S., Hirst, A. C., Jin, F. F., Wakata, Y., Yamagata, T., & Zebiak, S. E. (1998). ENSO theory. Journal of Geophysical Research: Oceans, 103(C7), 14261-14290.

57. Pant, G.B. and Parthasarathy, B., 1981. Some aspects of an association between the southern oscillation and Indian summer monsoon. Arch. Meteorol. Geophys. Biokl., Sr. B., 29, 245-251.

58. Parthasarathy, B., Rupa Kumar, K. and Munot, A.A., 1991b. Evidence of secular variations in Indian summer monsoon rainfall-circulation relationships. J. Climate, 4, 927-938.

59. Parthasarathy, B., K. R. Kumar, D. R. Kothawale, Indian summer monsoon rainfall indices: 1871–1990, Meteorol. Mag., 121, 174–186, 1992.

60. Parthasarathy, B., A. A. Munot, D. R. Kothawale, All-India monthly and summer rainfall indices: 1871–1993, Theor. Appl. Climatol., 49, 219–224, 1994.

61. Rasmusson, E. M., & Carpenter, T. H. (1983). The relationship between eastern equatorial Pacific sea surface temperatures and rainfall over India and Sri Lanka. Monthly Weather Review, 111(3), 517-528.

62. Rosatki A., Miakoda K., Gudgel R., (1997) The Impact of Ocean Initial Conditions on ENSO Forecasting with a Coupled Model. Monthly Weather Review, Jour. of Amer. Met. Soc., 125, 754-772.

63. Saravanan, R., 1993: Equatorial superrotation and maintenance of the general circulation in two-level models. J. Atmos. Sci., 50, 1211–1227.

64. Schwarzkopf, M. D., & Ramaswamy, V. (1999). Radiative effects of CH4, N2O, halocarbons and the foreign-broadened H2O continuum: A GCM experiment. Journal of Geophysical Research, 104(D8), 9467–9488. https://doi.org/10.1029/1999JD900003.

65. Shindell, D. T., G. A. Schmidt, M. E. Mann, and G. Faluvegi (2004a), Dynamic winter climate response to large tropical volcanic eruptions since 1600, Journal of Geophysical Research, 109, doi:10.1029/2003JD004151.

66. Shukla, J., & Paolino, D. A. (1983). The Southern Oscillation and long-range forecasting of the summer monsoon rainfall over India. Monthly Weather Review, 111(9), 1830-1837.

67. Singh, P., Chowdary, J. S., & Gnanaseelan, C. (2013). Impact of prolonged La Niña events on the Indian Ocean with a special emphasis on southwest Tropical Indian Ocean SST. Global and planetary change, 100, 28-37.

68. Seager, R., Harnik, N., Kushnir, Y., Robinson, W., & Miller, J. (2003). Mechanisms of hemispherically symmetric climate variability*. Journal of Climate, 16(18), 2960-2978.

69. Sterl, A., van Oldenborgh, G. J., Hazeleger, W., & Burgers, G. (2007). On the robustness of ENSO teleconnections. Climate Dynamics, 29(5), 469-485.

70. Schwendike, J., P. Govekar, M. J. Reeder, R. Wardle, G. J. Berry, and C. Jakob (2014), Local partitioning of the overturning circulation in the tropics and the connection to the Hadley and Walker circulations, Journal of Geophysical Research: Atmospheres, 119(3), 1322-1339.

71. Timmermann, A., Oberhuber, J., Bacher, A., Esch, M., Latif, M., & Roeckner, E. (1999). Increased El Niño frequency in a climate model forced by future greenhouse warming. Nature, 398(6729), 694-697.

72. Tokinaga, Hiroki, et al. "Slowdown of the Walker circulation driven by tropical Indo-Pacific warming." Nature 491.7424 (2012): 439-443.

73. Trenberth, K. E., Branstator, G. W., Karoly, D., Kumar, A., Lau, N. C., & Ropelewski, C. (1998). Progress during TOGA in understanding and modeling global teleconnections associated with tropical sea surface temperatures. Journal of Geophysical Research: Oceans, 103(C7), 14291-14324.

74. Trenberth KE, Caron JM (2000) The Southern Oscillation revisited: sea level pressure, surface temperatures, and precipitation. J Clim 13:4358–4365

75. Walker, G. T. (1925). Correlation in seasonal variations of WEATHER-A further study of world WEATHER 1. Monthly Weather Review, 53(6), 252-254.

76. Wang, C., Deser, C., Yu, J. Y., DiNezio, P., & Clement, A. (2012). El Niño and southern oscillation (ENSO): a review. Coral reefs of the Eastern Pacific, 3-19.

77. Wu, R., Lin, M., & Sun, H. (2020). Impacts of different types of El Niño and La Niña on northern tropical Atlantic sea surface temperature. *Climate Dynamics*, *54*(9), 4147-4167.

78. Wu, R., & He, Z. (2019). Northern tropical Atlantic warming in El Niño decaying spring: Impacts of El Niño amplitude. *Geophysical Research Letters*, *46*(23), 14072-14081.

79. Wu, R., Chen, J., & Chen, W. (2012). Different types of ENSO influences on the Indian summer monsoon variability. *Journal of Climate*, *25*(3), 903-920.

80. Xie, S. P., Deser, C., Vecchi, G. A., Ma, J., Teng, H., & Wittenberg, A. T. (2010). Global warming pattern formation: sea surface temperature and rainfall*. Journal of Climate, 23(4), 966-986.

81. Yeh, S. W., Kug, J. S., Dewitte, B., Kwon, M. H., Kirtman, B. P., & Jin, F. F. (2009). El Niño in a changing climate. Nature, 461(7263), 511-514.

82. Yu, J. Y., and S. T. Kim (2010), Three evolution, patterns of central Pacific El Niño, Geophys. Res. Lett., 37, L08706, doi:10.1029/2010GL042810.

83. Yu, R., & Zhou, T., 2004. Impacts of winter-NAO on March cooling trends over subtropical Eurasia continent in the recent century. Geophysical Research Letters, 31(L12204). doi: 10.1029/2004GL019814.

84. Zhao, M., I. M. Held, S.-J. Lin, and G. A. Vecchi (2009), Simulations of global hurricane climatology, interannual variability, and response to global warming using a 50-km resolution GCM, Journal of Climate, 22(24), 6653-6678.

85. Zhang, W. J., F.-F. Jin, J. P. Li, and H.-L. Ren, 2011: Contrasting impacts of two-type El Niño over the western North Pacific during boreal autumn. J. Meteor. Soc. Japan, 89, 563–569.

86. Zhang WJ, Jin FF, Ren HL, Li JP, Zhao JX (2012). Differences in teleconnection over the North Pacific and rainfall shift over the USA associated with two types of El Niño during boreal autumn. J Meteorol Soc Jpn 90:535–552

87. Zhang WJ, Jin FF, Zhao JX, Qi L, Ren HL (2013). The possible influence of a non-convectional El Niño on the severe autumn drought of 2009 in Southwest China. J Clim 26:8392–8405

88. Zhang, W., Wang, L., Xiang, B., Qi, L., & He, J. (2015). Impacts of two types of La Niña on the NAO during boreal winter. Climate Dynamics, 44(5-6), 1351-1366.

89. Zeng, N. (2003), Drought in the Sahel, Science, 302(5647), 999-1000.

Figure Legends:

Figure 1: Composited mean spatial pattern of 2m surface air temperature (°C in top) and precipitation (mm/day in bottom) in winter season produced using CFSR (left panel) and HiRAM simulation (right panel). Wind vectors are also overlaid from CFSR (left bottom panel) and HiRAM (right bottom panel).

Figure 2: Composited mean 2m surface temperature anomaly pattern from HiRAM (left panel) and CFSR (right panel) following strong El Niño and La Niña forcing in winter (DJF) season.

Figure 3: Composited mean precipitation (mm/d) anomaly following strong El Niño and La Niña forcing in winter (DJF) season.

Figure 4: Composited mean anomaly of zonal mean vertical velocity (Pa/s; in shaded colors) in the latitude pressure plane with overlaid zonal mean wind vectors (v; -100*omega) [m/s; 100*Pa/s] anomaly response following strong El Niño and La Niña forcing in winter (DJF) season. The length and direction of arrows depict the intensity (m/s) and direction of air movement in the latitude pressure plane respectively.

Figure 5: Composited mean meridional-mean (20S-20N) anomaly of vertical velocity (Pa/s) in the longitude pressure plane with overlaid meridional averaged (20°S-20°N) wind vectors (u; -1000*omega) [m/s; 1000*Pa/s] anomaly response in HiRAM (left panel) and CFSR (right panel) following strong El Niño and La Niña forcing in winter (DJF) season. The length and direction of arrows depict the intensity (m/s) and direction of air movement in the longitude pressure plane.

Figure 6: Composited mean geopotential height anomaly at 850-hPa following strong El Niño and La Niña forcing in winter (DJF) season.

Figure 7: Composited mean geopotential height anomaly at 200-hPa following strong El Niño and La Niña forcing in winter (DJF) season.

Figure 8: Composited mean 2m surface temperature anomaly pattern following weak El Niño and La Niña forcing in winter (DJF) season.

Figure 9: Composited mean precipitation (mm/d) anomaly following weak El Niño and La Niña forcing in winter (DJF) season.

Figure 10: Composited mean anomaly of zonal mean vertical velocity (Pa/s; in shaded colors) in the latitude pressure plane with overlaid zonal mean wind vectors (v; -100*omega) [m/s; 100*Pa/s] anomaly response following weak El Niño and La Niña forcing in winter (DJF) season. The length and direction of arrows depict the intensity (m/s) and direction of air movement in the latitude pressure plane respectively.

Figure 11: Composited mean meridional-mean (20°S-20°N) anomaly of vertical velocity (Pa/s) in the longitude pressure plane with overlaid meridional averaged (20°S-20°N) wind vectors (u; -1000*omega) [m/s; 1000*Pa/s] anomaly response following weak El Niño and La Niña forcing in winter (DJF) season. The length and direction of arrows depict the intensity (m/s) and direction of air movement in the longitude pressure plane.

Figure 12: Composited mean geopotential height anomaly at 850-hPa following weak El Niño and La Niña forcing in winter (DJF) season.

Figure 13: Composited mean geopotential height anomaly at 200-hPa following weak El Niño and La Niña forcing in winter (DJF) season.

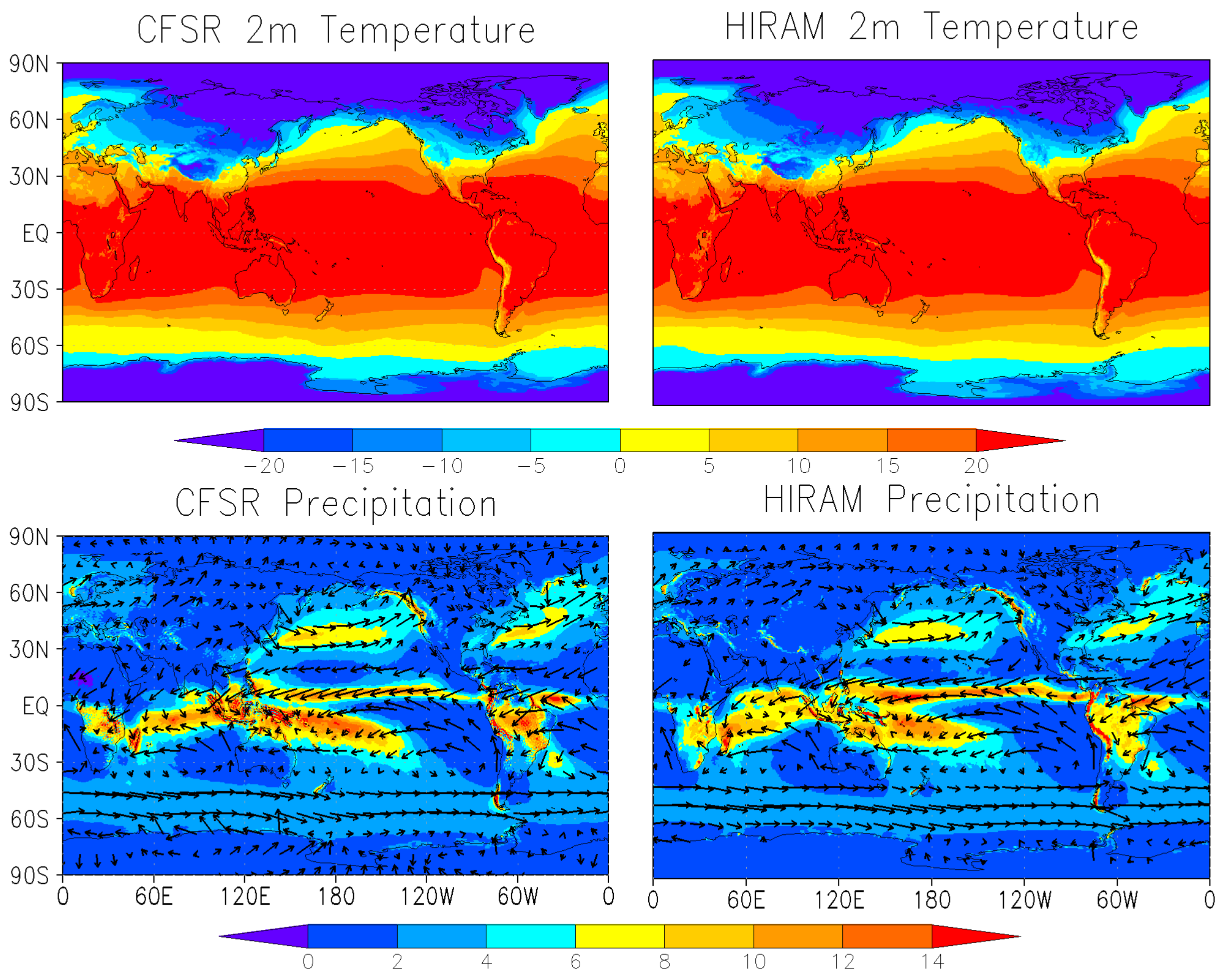

Figure 1: Composited mean spatial pattern of 2m surface air temperature (°C in top) and precipitation (mm/day in bottom) in winter season produced using CFSR (left panel) and HiRAM simulation (right panel). Wind vectors are also overlaid from CFSR (left bottom panel) and HiRAM (right bottom panel).

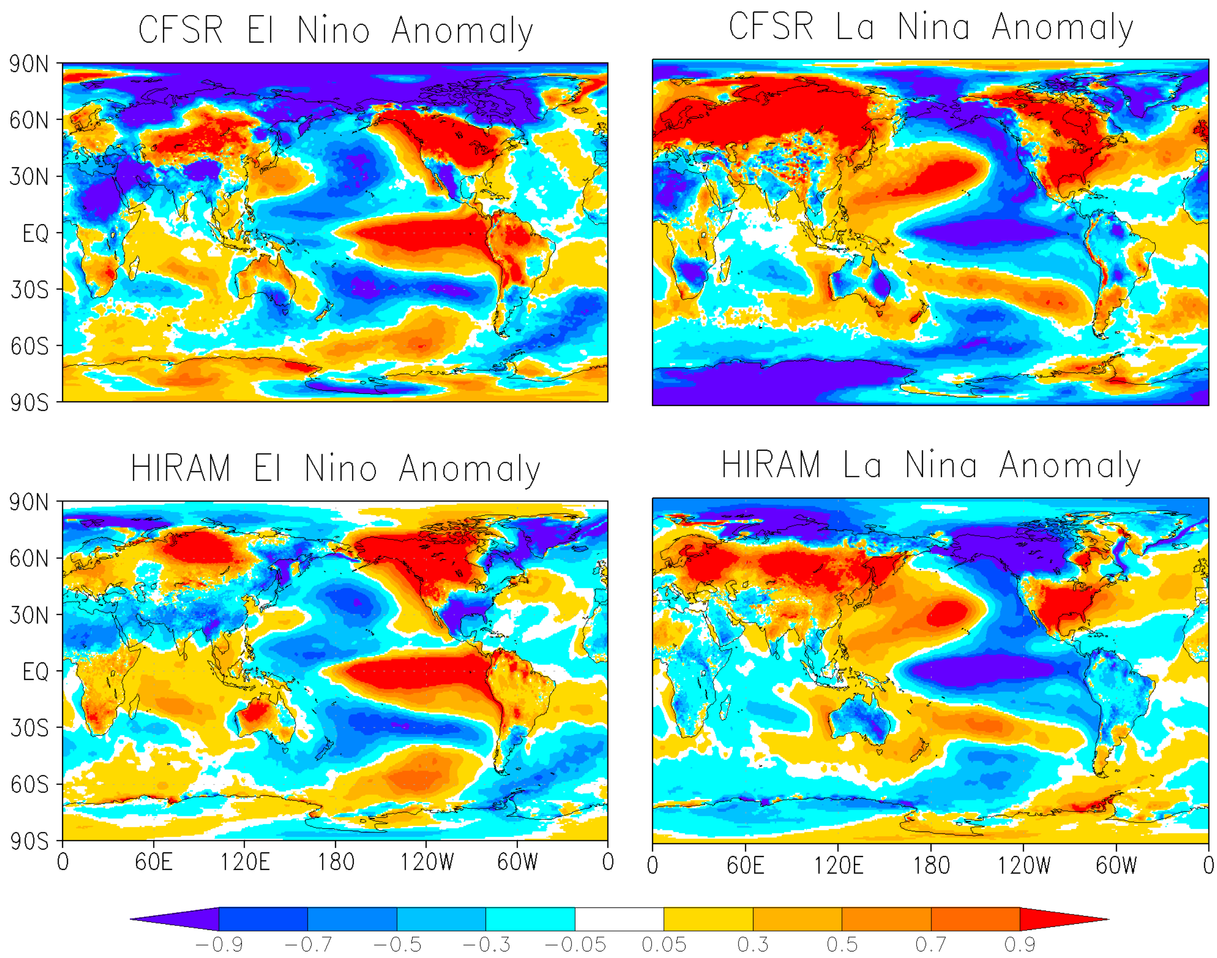

Figure 2: Composited mean 2m surface temperature anomaly pattern from HiRAM (left panel) and CFSR (right panel) following strong El Niño and La Niña forcing in winter (DJF) season.

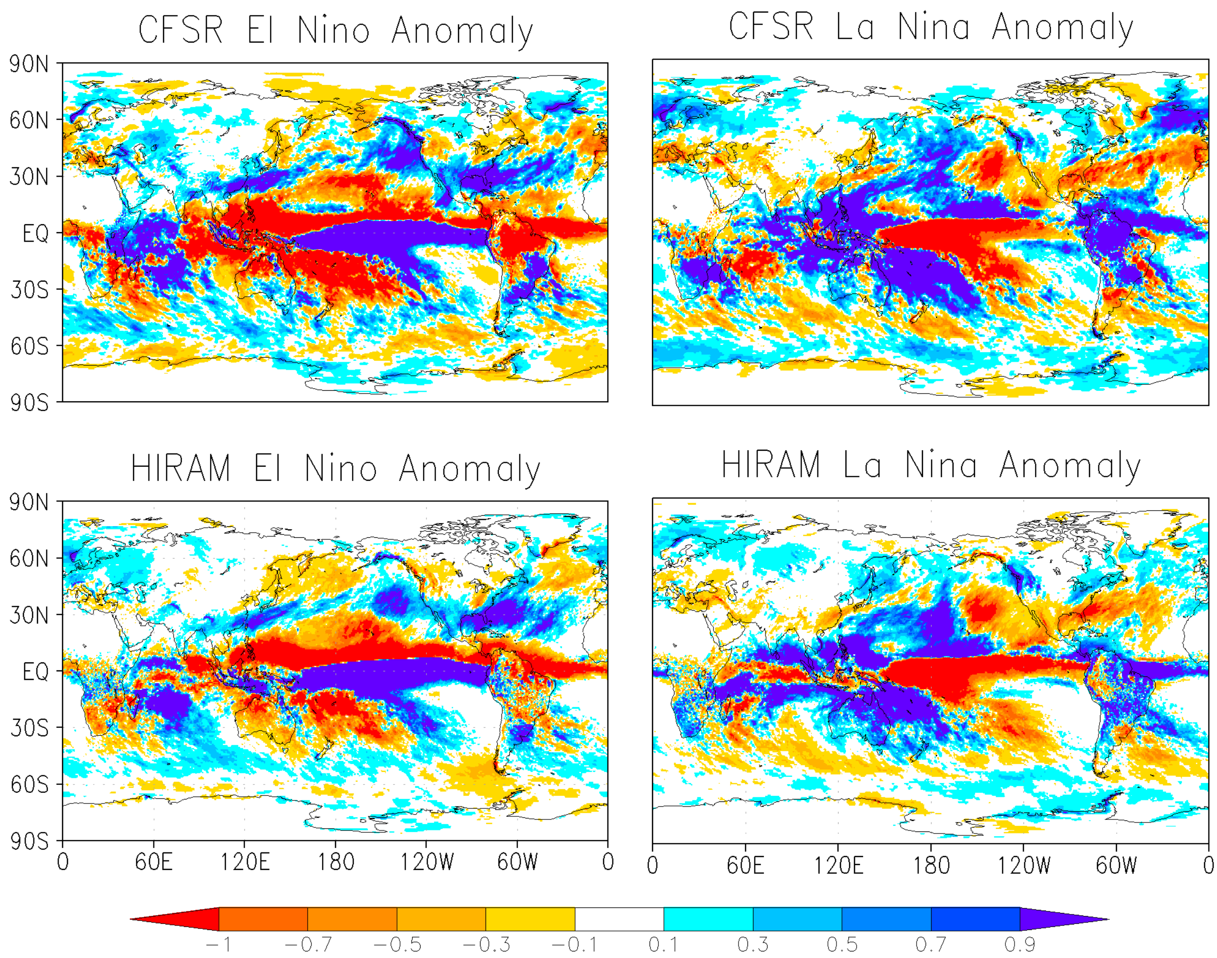

Figure 3: Composited mean precipitation (mm/d) anomaly from HiRAM (left panel) and CFSR (right panel) following strong El Niño and La Niña forcing in winter (DJF) season.

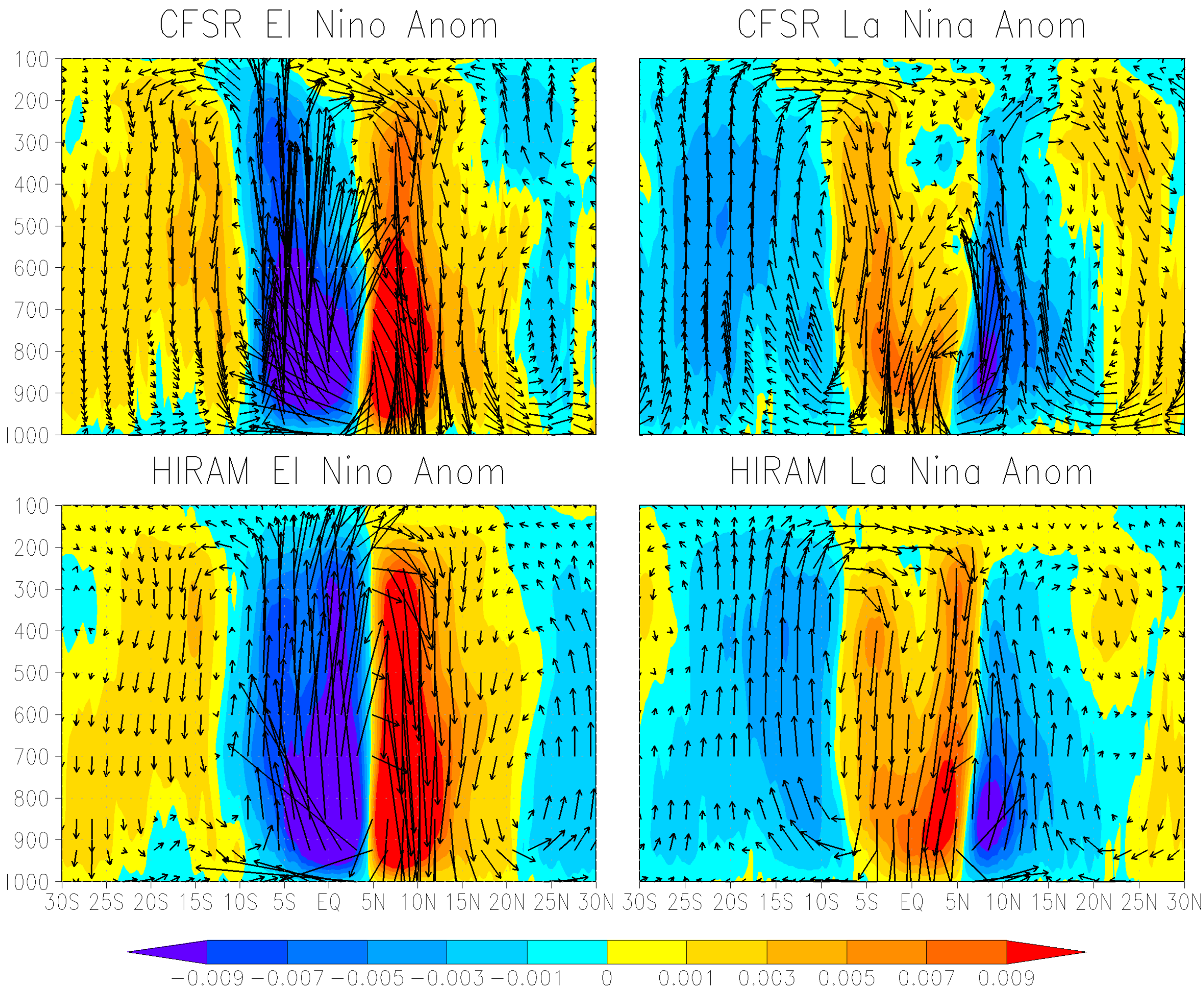

Figure 4: Composited mean anomaly of zonal mean vertical velocity (Pa/s; in shaded colors) in the latitude pressure plane with overlaid zonal mean wind vectors (v; -100*omega) [m/s; 100*Pa/s] anomaly response in HiRAM (left panel) and CFSR (right panel) following strong El Niño and La Niña forcing in winter (DJF) season. The length and direction of arrows depict the intensity (m/s) and direction of air movement in the latitude pressure plane respectively.

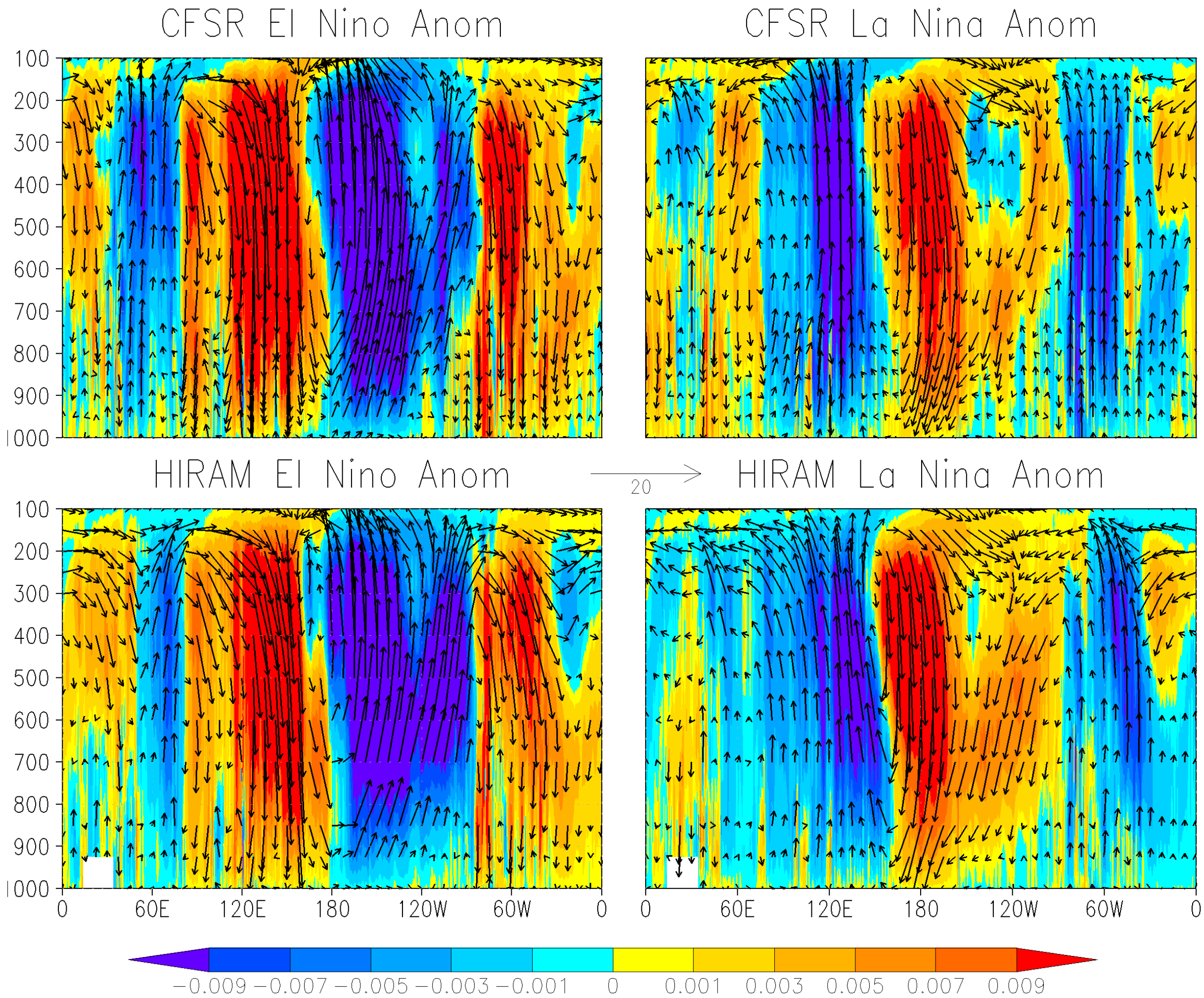

Figure 5: Composited mean meridional-mean (20°S-20°N) anomaly of vertical velocity (Pa/s) in the longitude pressure plane with overlaid meridional averaged (20°S-20°N) wind vectors (u; -1000*omega) [m/s; 1000*Pa/s] anomaly response in HiRAM (left panel) and CFSR (right panel) following strong El Niño and La Niña forcing in winter (DJF) season. The length and direction of arrows depict the intensity (m/s) and direction of air movement in the longitude pressure plane.

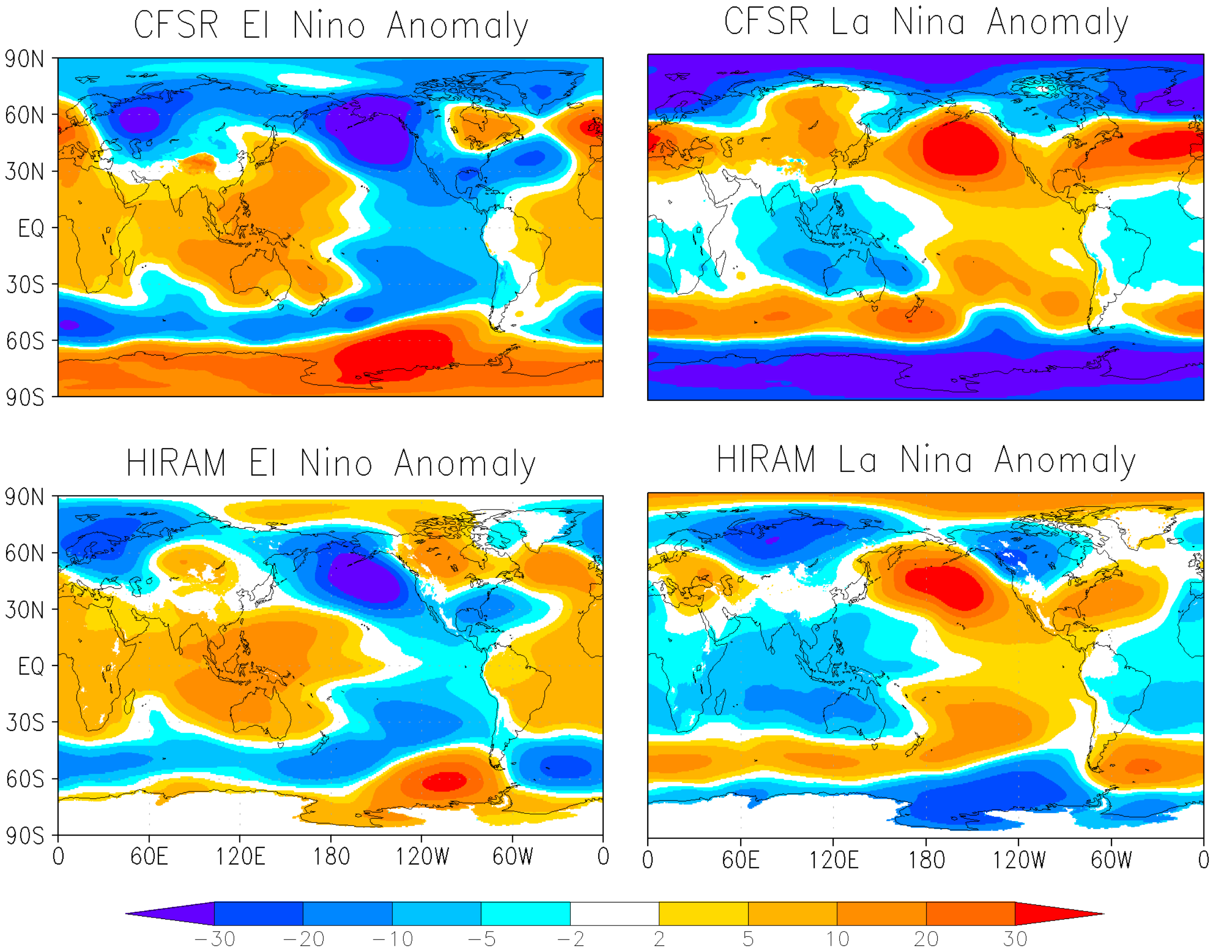

Figure 6: Composited mean geopotential height anomaly at 850-hPa following strong El Niño and La Niña forcing in winter (DJF) season.

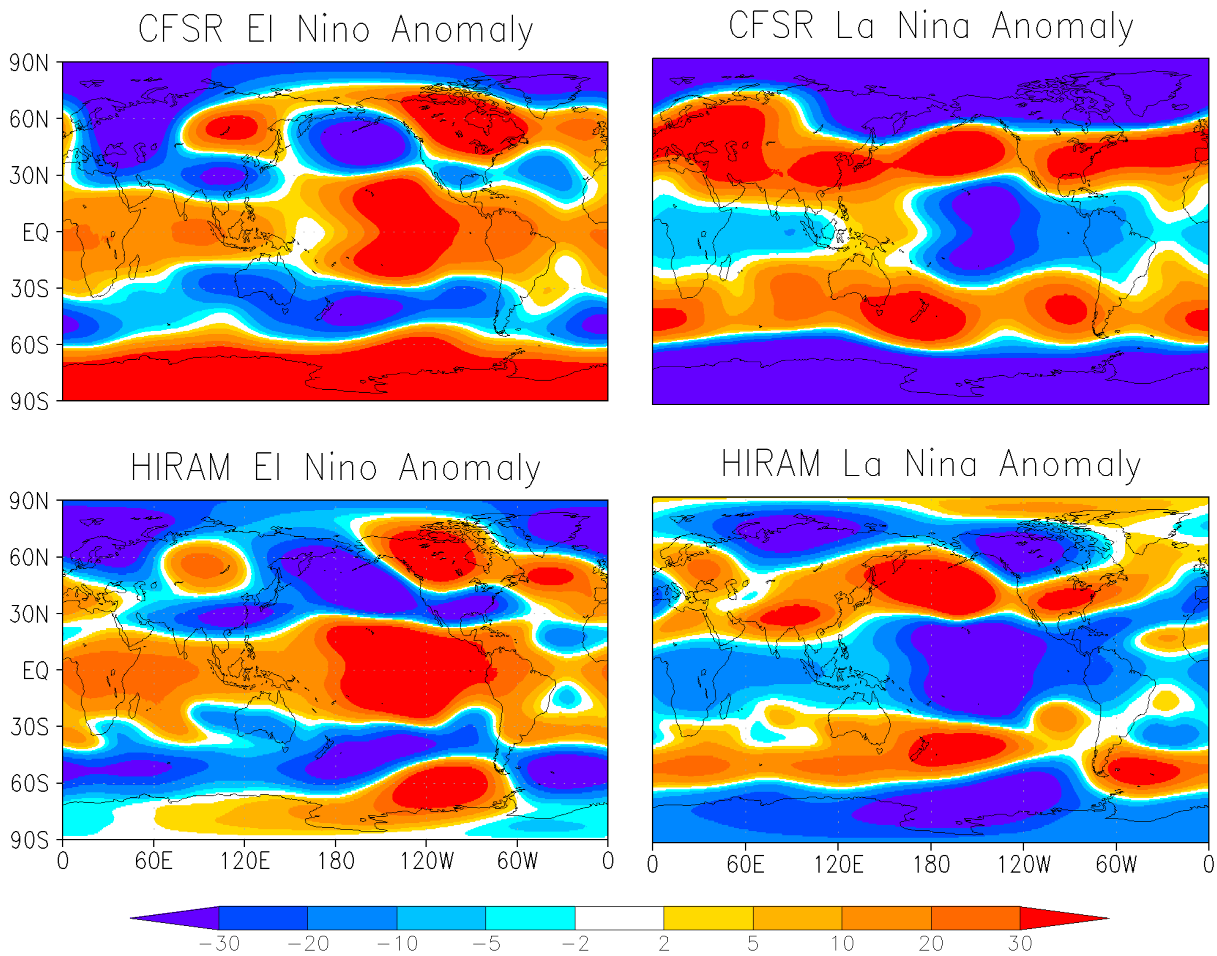

Figure 7: Composited mean geopotential height anomaly at 200-hPa following strong El Niño and La Niña forcing in winter (DJF) season.

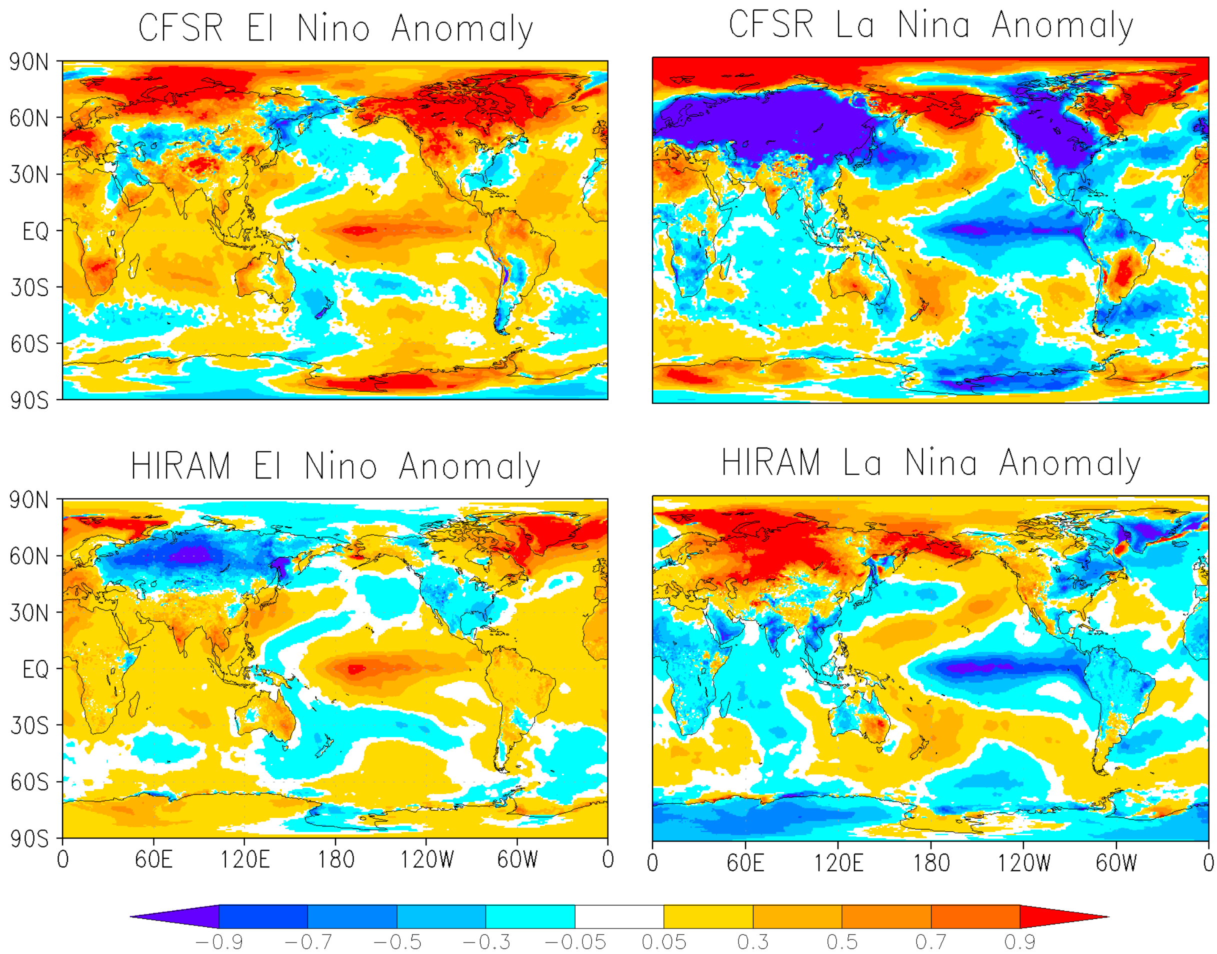

Figure 8: Composited mean 2m surface temperature anomaly pattern following weak El Niño and La Niña forcing in winter (DJF) season.

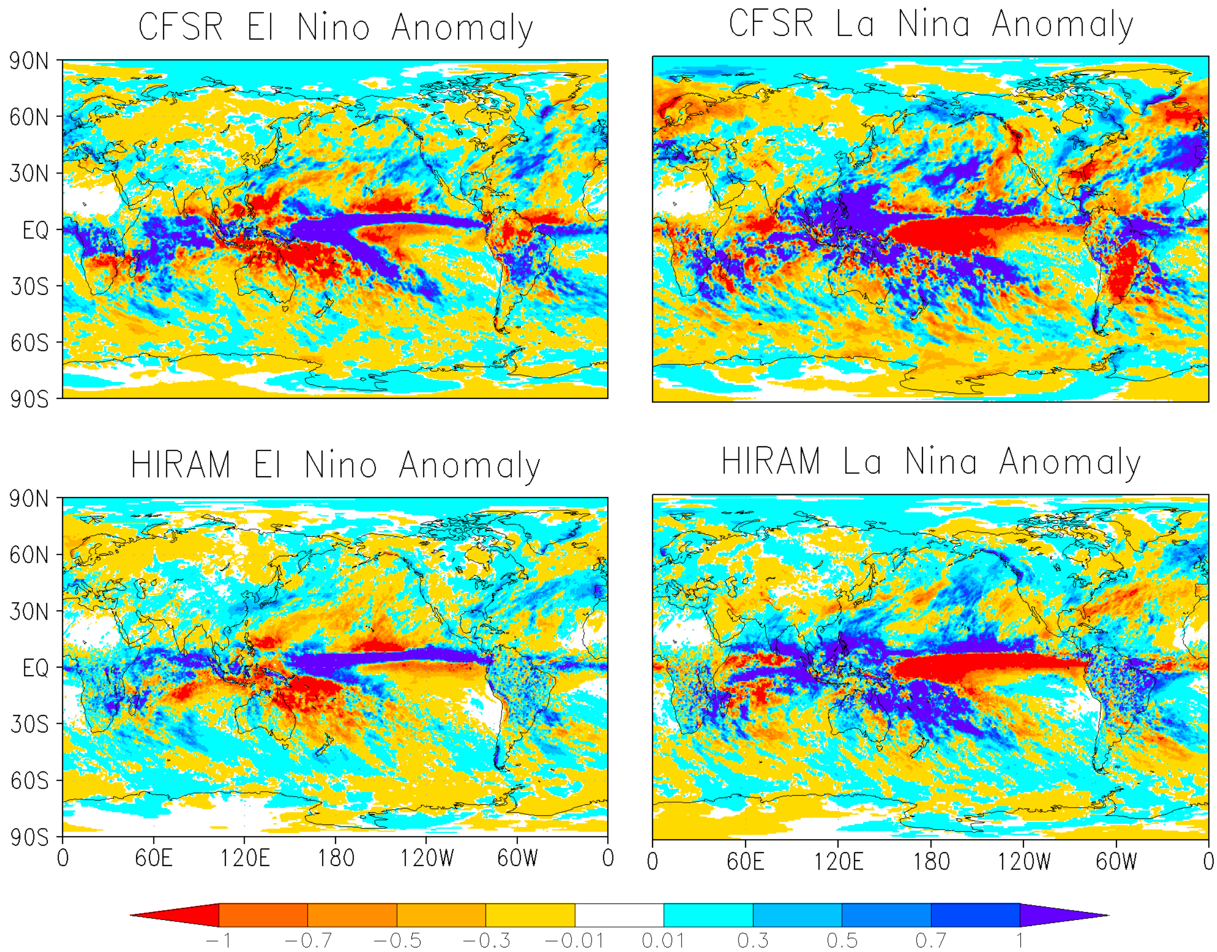

Figure 9: Composited mean precipitation (mm/d) anomaly following weak El Niño and La Niña forcing in winter (DJF) season.

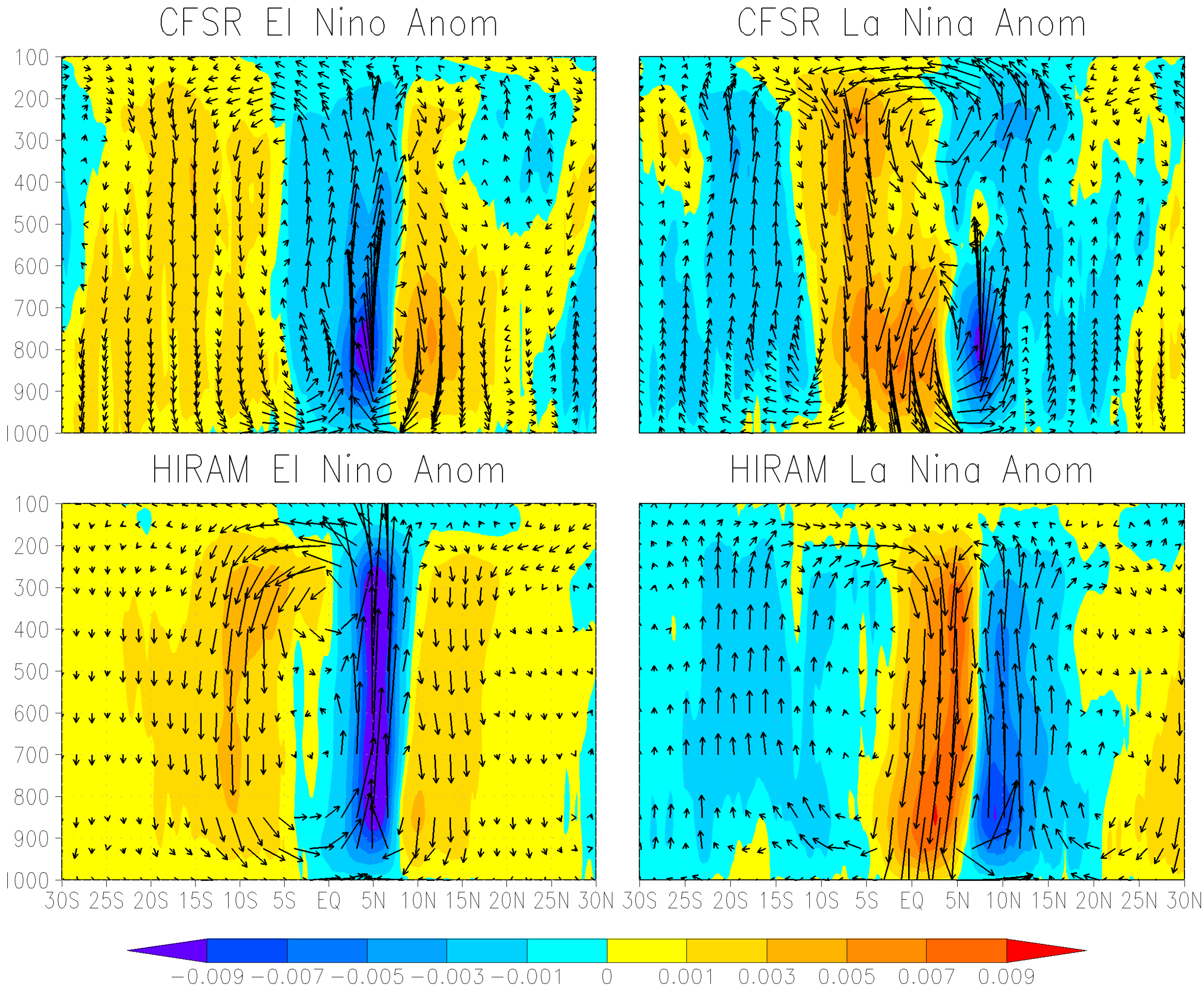

Figure 10: Composited mean anomaly of zonal mean vertical velocity (Pa/s; in shaded colors) in the latitude pressure plane with overlaid zonal mean wind vectors (v; -100*omega) [m/s; 100*Pa/s] anomaly response in HiRAM (left panel) and CFSR (right panel) following weak El Niño and La Niña forcing in winter (DJF) season. The length and direction of arrows depict the intensity (m/s) and direction of air movement in the latitude pressure plane respectively.

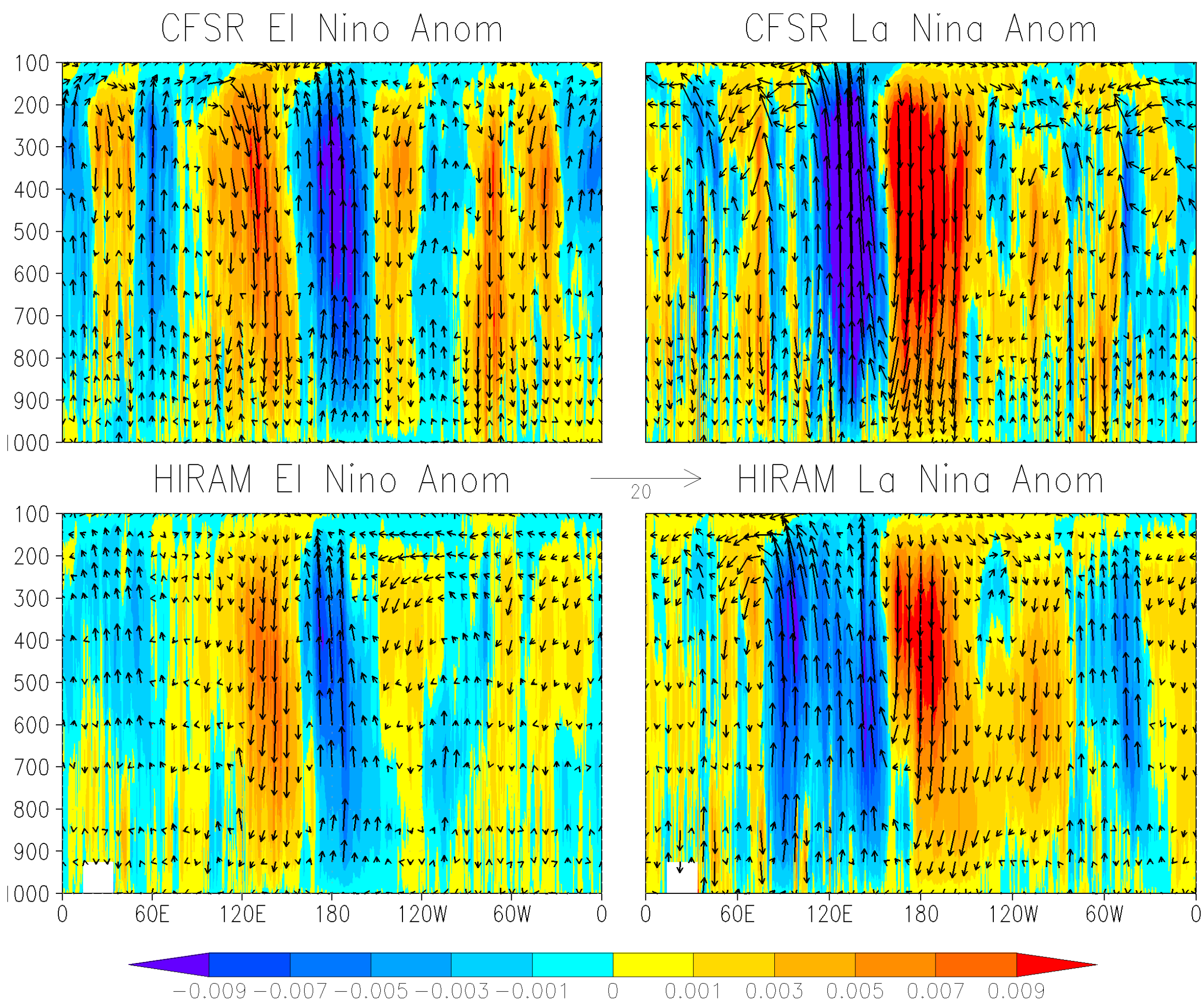

Figure 11: Composited mean anomaly of meridional-mean (20°S-20°N) vertical velocity (Pa/s) in the longitude pressure plane with overlaid meridional averaged (20°S-20°N) wind vectors (u; -100*omega) [m/s; 100*Pa/s] anomaly response in HiRAM (left panel) and CFSR (right panel) following weak El Niño and La Niña forcing in winter (DJF) season. The length and direction of arrows depict the intensity (m/s) and direction of air movement in the longitude pressure plane.

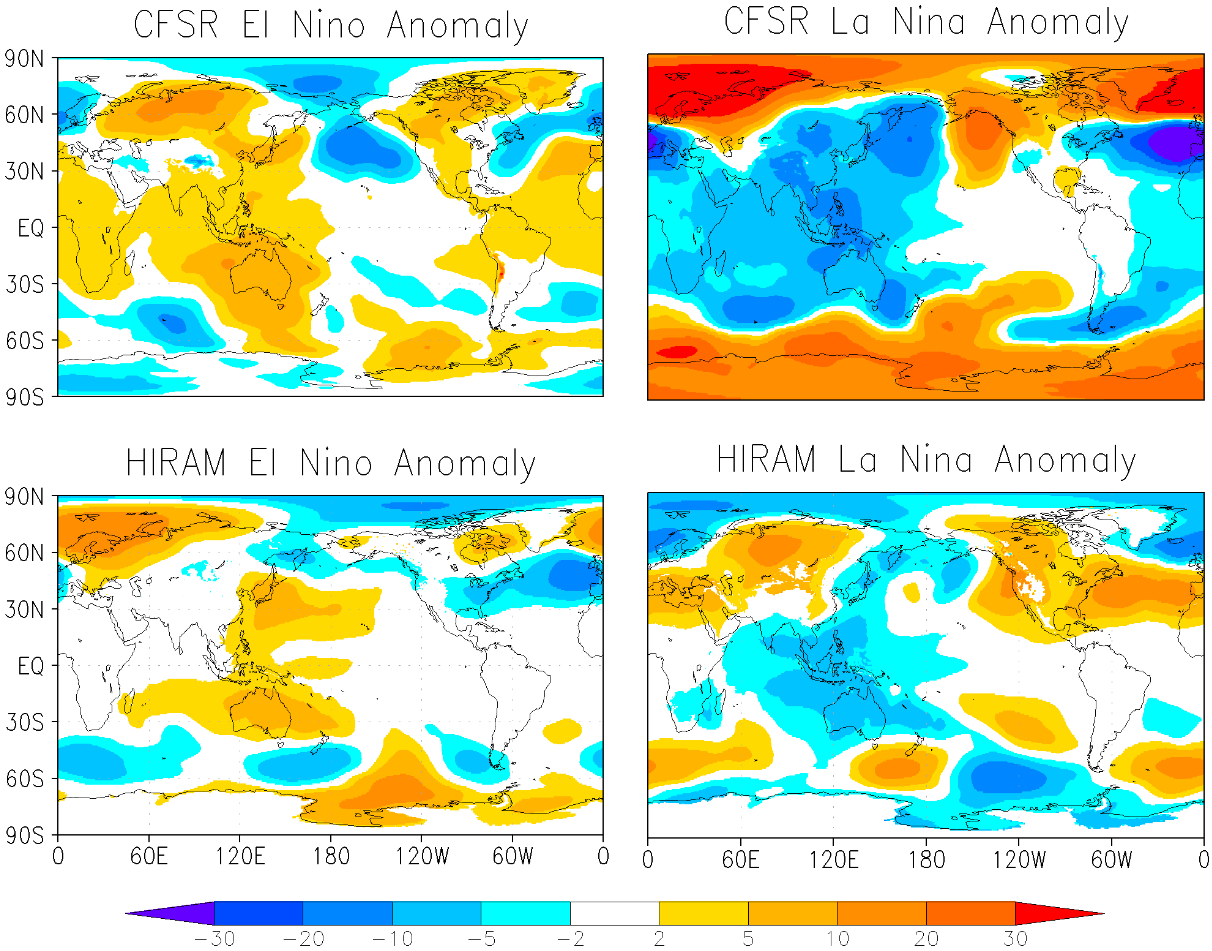

Figure 12: Composited mean geopotential height anomaly at 850-hPa following weak El Niño and La Niña forcing in winter (DJF) season.

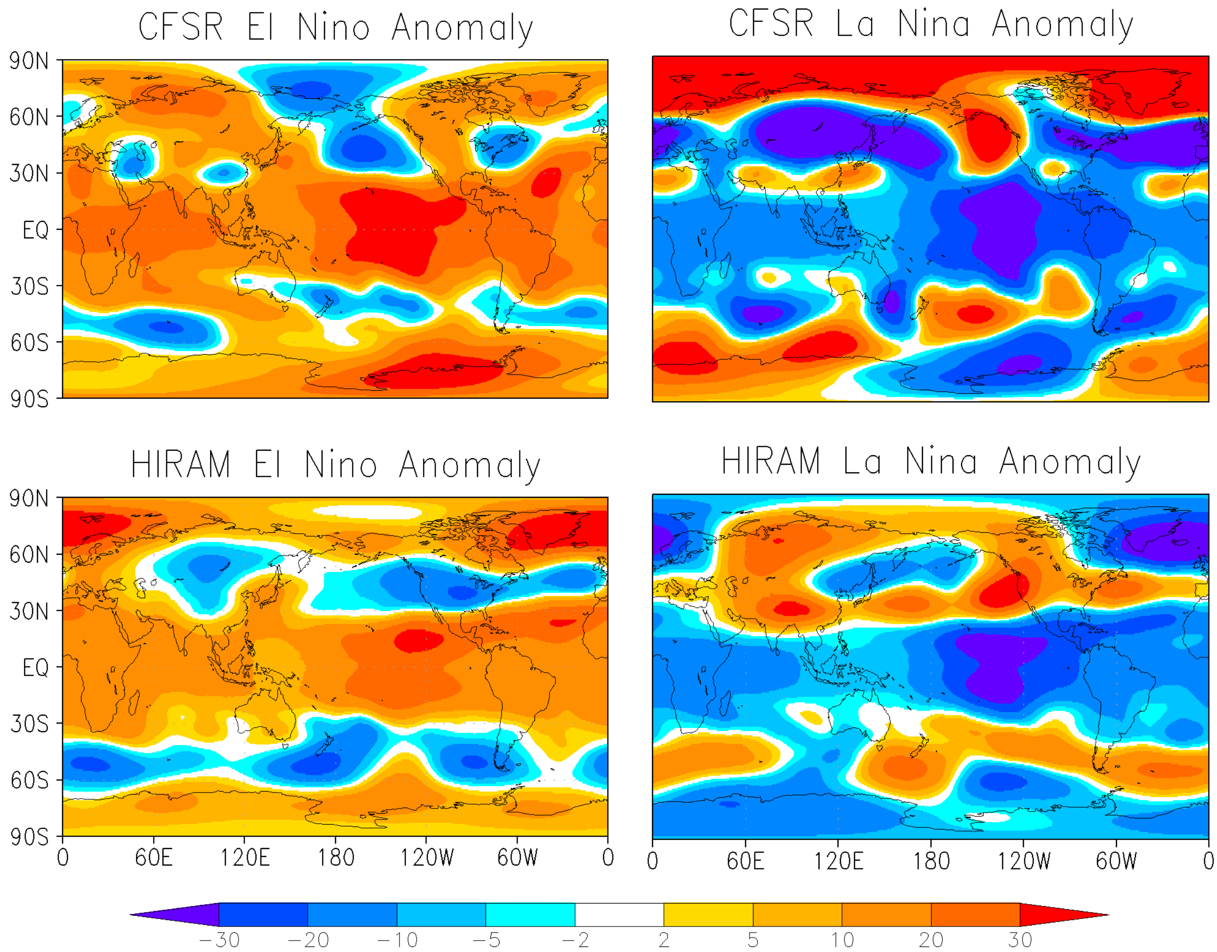

Figure 13: Composited mean geopotential height anomaly at 200-hPa following weak El Niño and La Niña forcing in winter (DJF) season.

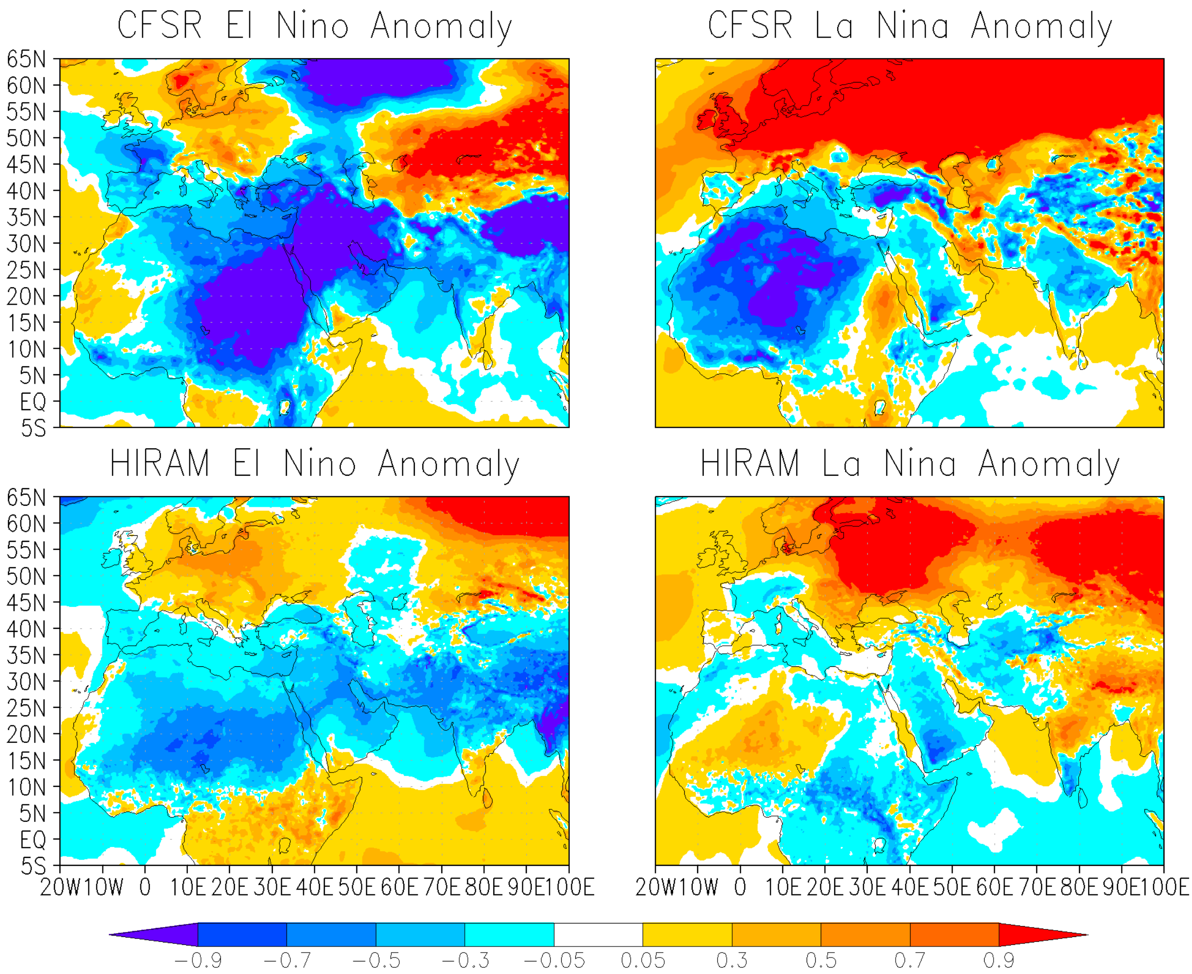

Figure 14: Composited mean surface temperature anomaly following strong El Niño and La Niña forcing over MENA region in winter (DJF) season.

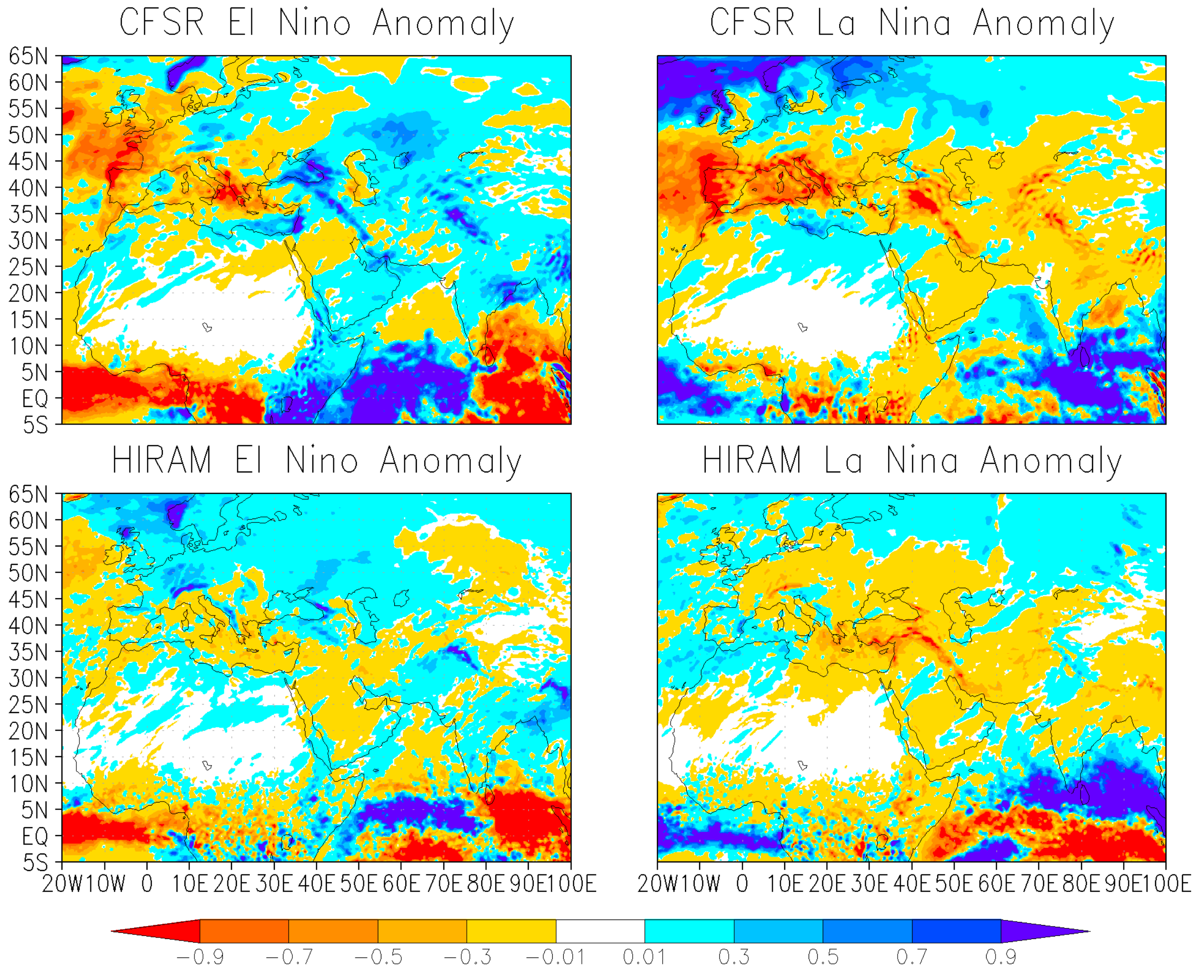

Figure 15: Composited mean precipitation anomaly following strong El Niño and La Niña forcing over MENA region in winter (DJF) season.

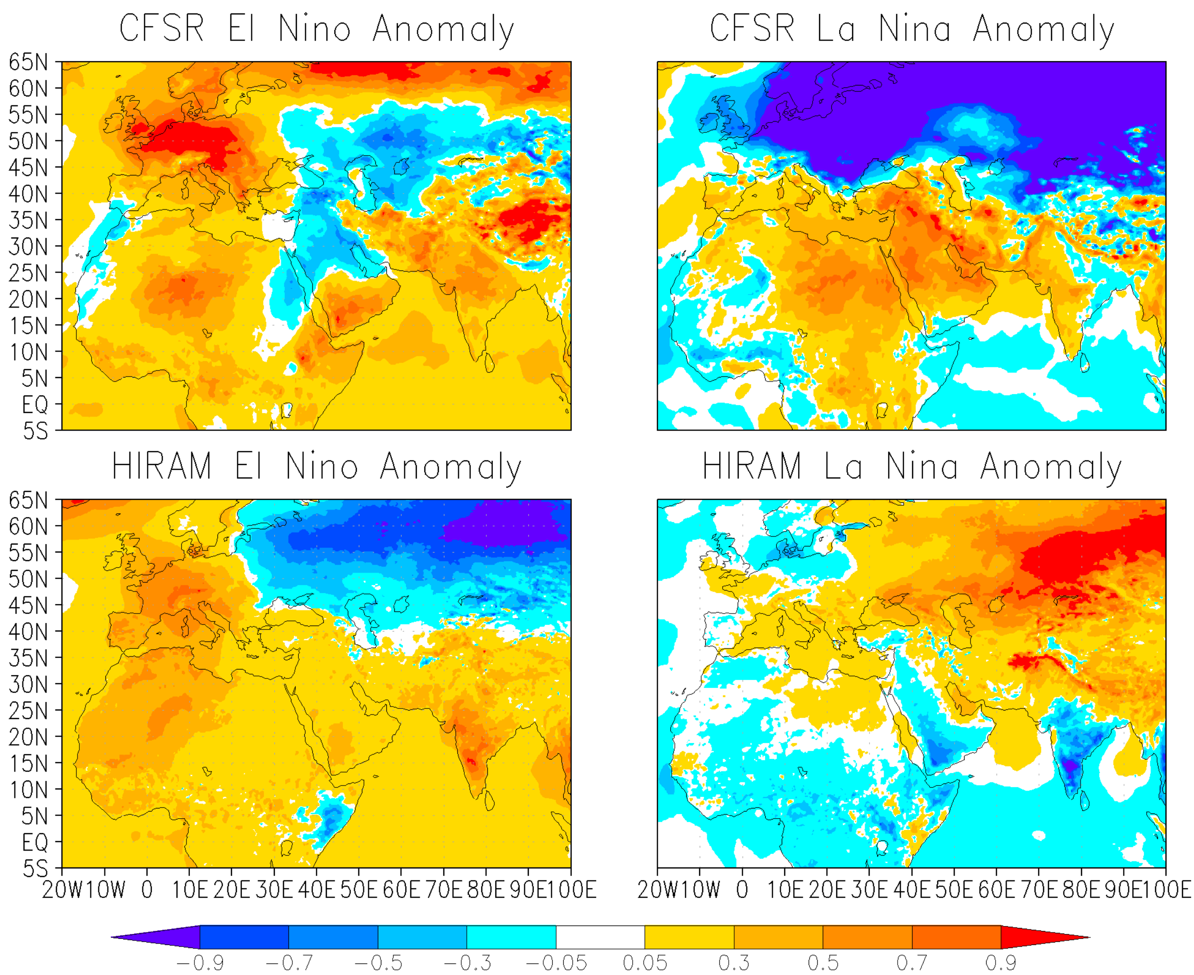

Figure 16: Composited mean surface 2m temperature anomaly following weak El Niño and La Niña forcing over MENA region in winter (DJF) season.

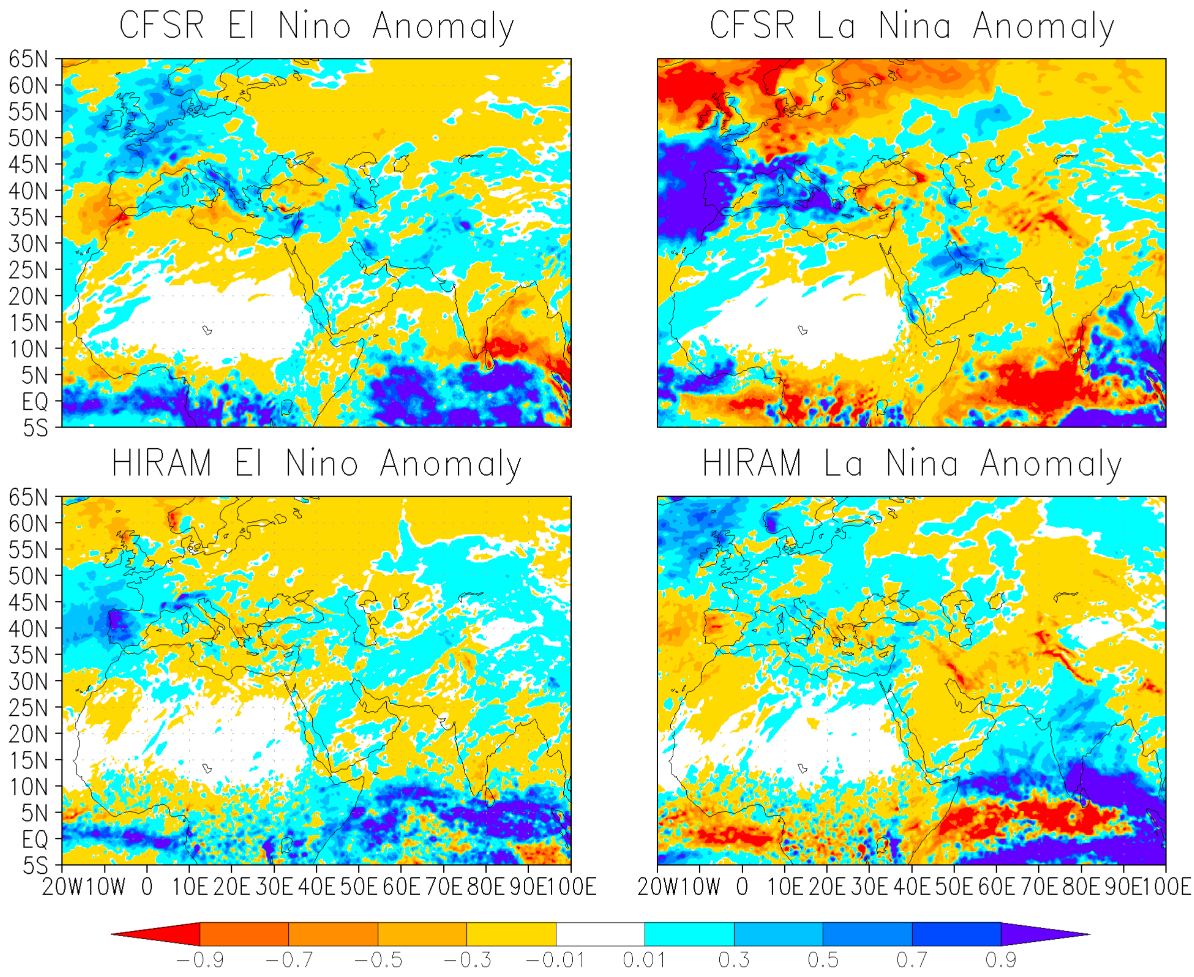

Figure 17: Composited mean precipitation anomaly following weak El Niño and La Niña forcing over MENA region in winter (DJF) season.